J. Fluid Mech. (1984), *vol.* 146, *pp.* 417–449
Printed in Great Britain

Proximity-induced galloping of two interfering circular cylinders

By A. BOKAIAN†
Earl and Wright Ltd, Consulting Engineers, Victoria Station House, 191 Victoria Street, London SW1E 5NE

AND F. GEOOLA
Department of Civil Engineering, University College London, Gower Street, London WC1E 6BT

(Received 16 November 1983 and in revised form 9 May 1984)

Experiments were conducted to investigate the response of a rigid two-dimensional elastically mounted smooth circular cylinder, with oscillations restricted to a plane normal to the incident flow, as influenced by the vicinity of an identical fixed body placed inside the wake. The static lift and drag coefficients, as well as the vibration amplitude and frequency of the upstream cylinder as functions of relative position of the pair of cylinders are given. Most measurements were carried out under two conditions of free-stream turbulence. Whilst turbulence decreased the magnitude of drag coefficients, it had no appreciable effect on lift coefficients. The forces on the upstream body were found to be influenced by the proximity to the downstream one in a significant way only when the streamwise spacing is less than two diameters.

In the dynamic tests, two kinds of instability, namely a vortex-resonance and galloping, were observed, with the latter only occurring when the downstream cylinder was well submerged in the near wake of the upstream one. The vortex-shedding frequency was always found to lock to oscillation frequency. Whereas the vibration characteristics remained essentially unaffected with changing turbulence intensity, the galloping amplitudes were observed to be sensitive to cylinders' aspect ratio. A quasi-steady theory was developed to predict the galloping behaviour.

1. Introduction

When a single elastic circular cylinder subjected to a uniform flow vibrates in a cross-flow direction, the flow field becomes complex because of the interaction of the fluid flow and the body motion. When this cylinder is approached from a downstream direction by a similar bluff body which is held fixed and parallel in the near wake of the upstream cylinder, the flow field and the dynamic response of the front (upstream) body becomes significantly more complex as a result of mutual interaction between the two cylinders. This means, amongst other things, that the critical flow speed corresponding to the vibration onset may change, the oscillation amplitude also intensifies and may become excessive. In general, above a critical threshold flow velocity, the amplitude of motion grows consistently with increasing flow speed, thus resembling the galloping instability of isolated non-circular cylinders. The present paper describes an experimental and analytical investigation into the response of a rigid two-dimensional elastically mounted smooth circular cylinder, having oscillations restricted to a plane normal to the incident flow, with a stationary identical parallel cylinder placed inside its wake.

† Formerly at London Centre for Marine Technology.

The work that instigated the present research was first undertaken by Zdravkovich (1974) when he was trying to obtain insight into the flow-induced vibrations of two interfering circular cylinders. He carried out some tests in an open-circuit wind tunnel on a pair of identical rigid cylinders in tandem arrangement (the line connecting the cylinder centres being parallel to the flow direction) over a Reynolds-number range from about 1×10^5 to 2×10^5 (based on the diameter of a single cylinder), with the upstream cylinder flexibly mounted so as to have only a cross-flow vibration while the downstream body was being held stationary. He did not collect any quantitative information, and observed no large-amplitude oscillations except at the gap of 0.5 cylinder diameters, where serious self-excited vibrations occurred. Small-scale laboratory observations in this study have also indicated that, when the two bodies are in close proximity of one another with the rear (downstream) cylinder well inside the wake of the front one, the upstream cylinder is susceptible to galloping, and, depending on flow condition and the mass and structural damping of the cylinder, large-amplitude galloping-type oscillations can build up. The cylinder vibrates more severely as the downstream cylinder is brought closer to it. However, once the gap between the two bodies exceeds a few diameters, the fixed downstream cylinder can practically have no effect on the fluid-dynamic excitations of the upstream one; the upstream body then could only suffer from an ordinary vortex resonance. For these reasons, the abovementioned type of instability will be referred to as 'proximity galloping'. Most recently, Ruscheweyh (1983) carried out some interesting wind-tunnel experiments with a pair of identical smooth circular cylinders at a Reynolds number of the order of 9×10^4. The individual cylinders were mounted in order to have a two degrees of freedom oscillation. His research was in relation to wind-excited instability of stacks. At the gap of 0.5 diameters, and when the incident flow was at an angle of 10° with respect to the line connecting the cylinder centres (a slightly staggered arrangement), both cylinders exhibited a large-amplitude galloping-type oscillation, with the upstream one undergoing a predominantly transverse motion. In Zdravkovich's observations, only the gross characteristics of the problem were studied, with very little attention being given to the flow processes. A better understanding of these gross characteristics should result in a more rational and economical design procedure for two interfering circular cylinders.

The principal aim of the present study was to quantify the fluid-elastic instabilities of the upstream cylinder, both in amplitude and frequency domains, in terms of governing flow and structural parameters and the relative position with respect to the fixed downstream body. The two cylinders were located at various distances from each other in-line and across-flow. A quasi-steady theory was developed for the prediction of the oscillation amplitude and frequency. With both cylinders stationary, observations were made as to the way in which the lift and drag coefficients of the upstream cylinder changed, as the cylinders' separation was reduced, from that of two independent cylinders to that of an almost single body. The measurements thus obtained were used in the theoretical prediction procedure, and the results were discussed in terms of the observed dynamic test data.

2. Mathematical model

Figure 1 represents a two-dimensional flow of velocity V streaming past two neighbouring identical parallel circular cylinders of diameter D. The downstream body is held fixed while the upstream one is constrained to move only vertically at right angles to the flow direction. In this figure s and r represent the longitudinal and

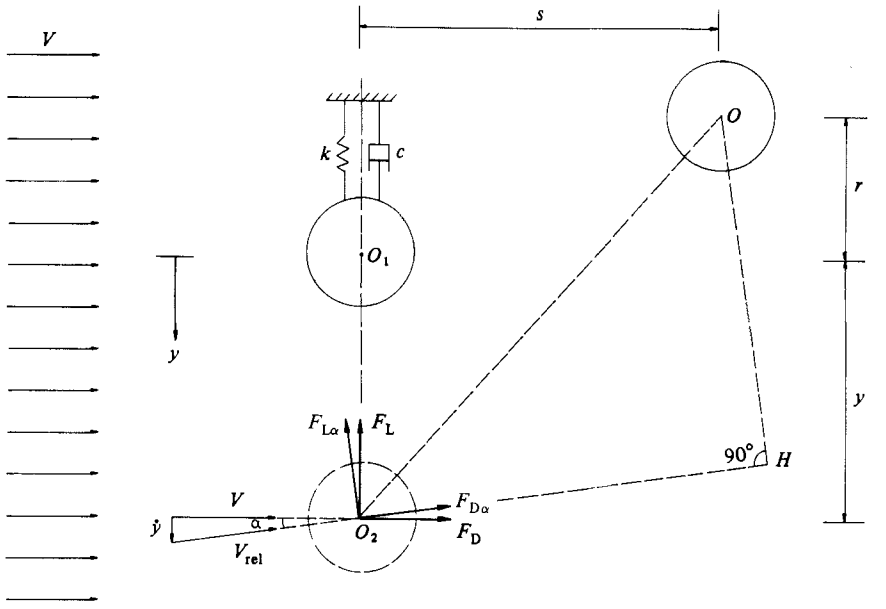

FIGURE 1. Vibrating circular cylinder in proximity to a stationary downstream neighbour.

transverse spacing between the centre of the rear cylinder and that of the front one in its mean position. These two quantities are made dimensionless by dividing them by the cylinder diameter to give the relative streamwise and lateral separations $x_0 = s/D$ and $y_0 = r/D$ respectively. When the vibrating body moves downwards with velocity $\dot{y}$, the relative velocity between the oncoming steady flow and the oscillating cylinder is given by V_{rel} in the triangle of velocities drawn. This relative flow velocity V_{rel} at an angle of attack $\alpha = \tan^{-1}(\dot{y}/V)$ will give rise to a transverse component of force F_y. With this, the differential equation of motion about the equilibrium position of the elastically suspended cylinder may be expressed as

$$m\ddot{y} + c\dot{y} + ky = F_y. \tag{1}$$

m is the total vibrating mass (mass of the system in still fluid plus the added mass); y is the downward displacement from the equilibrium position; c indicates the usually small, linear damping; k denotes a linear spring constant (the stiffness), and an overdot represents differentiation with respect to time.

The fluid-dynamic forces are obtained using a quasi-steady hypothesis, in which the lateral force F_y is assumed to be the same as on a fixed body during a static test under the same angle of flow attack and the same longitudinal and lateral spacing. At any moment during the oscillation, the relative transverse separation of the vibrating cylinder from the fixed downstream body is $y_0 + y/D$. The moving cylinder experiences a force having two components of drag $F_{D\alpha}$ and lift $F_{L\alpha}$ acting along and normal to the relative velocity vector respectively, as shown in figure 1. By resolving the lift and drag forces in the y-direction, it may be written

$$m\ddot{y} + c\dot{y} + ky = F_y = -\tfrac{1}{2}\rho DLV_{\text{rel}}^2 (C_{D\alpha}\sin\alpha + C_{L\alpha}\cos\alpha), \tag{2}$$

where ρ and L indicate the fluid density and the cylinder length respectively, and $C_{D\alpha} = F_{D\alpha}/(\frac{1}{2}\rho DLV_{\text{rel}}^2)$ and $C_{L\alpha} = F_{L\alpha}/(\frac{1}{2}\rho DLV_{\text{rel}}^2)$ denote respectively the drag and lift coefficients based on the relative velocity V_{rel} and the separations O_2H and OH.

By introducing the independent variables of natural circular frequency

$\omega_n = (k/m)^{\frac{1}{2}}$, the reduced displacement $Y = y/D$, the reduced damping $\beta = c/2m\omega_n$ and the mass parameter $n = \rho D^2 L/2m$, the equation of motion may be written as

$$\ddot{Y} + 2\omega_n \beta \dot{Y} + \omega_n^2 Y = -\frac{nV}{D}\left(C_{D\alpha}\dot{Y} + C_{L\alpha}\frac{V}{D}\right). \tag{3}$$

The above relationship is valid only when the angle α is small; that is, when the cylinder velocity $\dot{y}$ at the relative separation x_0 and y_0 is much smaller than the free-stream velocity V.

In figure 1 F_D and F_L represent the static drag and lift forces for the relative longitudinal and transverse spacing of x_0 and $y_0 + Y$ under the free-stream velocity V (the zero angle of flow attack). The lift and drag coefficients $C_D = F_D/(\frac{1}{2}\rho DLV^2)$ and $C_L = F_L/(\frac{1}{2}\rho DLV^2)$ are related to the coefficients $C_{D\alpha}$ and $C_{L\alpha}$ by the following relationships:

$$C_{D\alpha} = C_D + \frac{\partial C_D}{\partial x_0}\delta x_0 + \frac{\partial C_D}{\partial (y_0 + Y)}\delta(y_0 + Y), \tag{4}$$

$$C_{L\alpha} = C_L + \frac{\partial C_L}{\partial x_0}\delta x_0 + \frac{\partial C_L}{\partial (y_0 + Y)}\delta(y_0 + Y), \tag{5}$$

in which δx_0 and $\delta(y_0 + Y)$ are defined as

$$\delta x_0 = \frac{O_2 H \cos\alpha}{D} - x_0 = 0.5[(y_0 + Y)\sin 2\alpha + x_0(\cos 2\alpha - 1)], \tag{6}$$

$$\delta(y_0 + Y) = \frac{OH\cos\alpha}{D} - (y_0 + Y) = 0.5[(y_0 + Y)(\cos 2\alpha - 1) - x_0 \sin 2\alpha]. \tag{7}$$

With the assumption of α being small, δx_0 and $\delta(y_0 + Y)$ are simplified as

$$\delta x_0 = \frac{D(y_0 + Y)\dot{Y}}{V}, \quad \delta(y_0 + Y) = -\frac{Dx_0 \dot{Y}}{V}. \tag{8), (9}$$

Using the relationships (4), (5), (8) and (9), the differential equation of motion (3) is transformed into

$$\ddot{Y} + \omega_n^2 Y = -n\omega_n U\left[C_D \dot{Y} + \omega_n U C_L - x_0 \dot{Y}\frac{\partial C_L}{\partial (y_0 + Y)} + (Y + y_0)\dot{Y}\frac{\partial C_L}{\partial x_0} + \frac{2\beta}{nU}\dot{Y}\right], \tag{10}$$

in which $U = V/\omega_n D$ is the reduced velocity. In the above relationship, the terms $\omega_n^2 Y + n\omega_n^2 U^2 C_L$ indicate variations in the oscillation frequency of the cylinder, while the 'damping effect' is from the following expression:

$$\left[C_D - x_0\frac{\partial C_L}{\partial (y_0 + Y)} + (Y + y_0)\frac{\partial C_L}{\partial x_0} + \frac{2\beta}{nU}\right] n\omega_n U. \tag{11}$$

The self-excitation will begin when the above expression becomes negative.

The static lift and drag forces on the front cylinder are functions of the cylinders' spacing. Since the lift coefficient is antisymmetrical with respect to the wake centreline, its variation can, for example, be approximated by a polynomial in x_0 of degree I and in $Y + y_0$ of degree $2K + 1$, where I and K are integers. Thus

$$C_L = \sum_{i=0}^{K}\sum_{j=0}^{I} A_{(2i+1,j)} x_0^j (Y + y_0)^{2i+1}, \tag{12}$$

in which i and j are counters and the $A_{(2i+1,j)}$ are constant coefficients. These coefficients are obtained by fitting a surface to the measured values of C_L for a set

of separations between the two cylinders. The variation of drag coefficient is symmetrical with respect to the wake centreline, and therefore can similarly be expressed by a power series in the form

$$C_{\mathrm{D}} = \sum_{i=0}^{M} \sum_{j=0}^{N} C_{(2i,j)} x_0^j (Y+y_0)^{2i}, \tag{13}$$

where M and N are integers denoting the degrees of the polynomial in $Y+y_0$ and x_0 respectively, and $C_{(2i,j)}$ are constant coefficients. They are obtained by a procedure similar to that described for the lift coefficient.

As the dynamic test observations in §4.3 will reveal, the galloping instability only occurs when the downstream cylinder is situated in the near-wake region of the upstream one. The lift- and drag-coefficients data, as will be shown in §4.5, indicate that in this region C_{L} can satisfactorily be approximated by a polynomial of degree 4 in terms of x_0 and of degree 5 in terms of $Y+y_0$. Hence

$$C_{\mathrm{L}} = \sum_{j=0}^{5} A_j Y^j, \tag{14}$$

where

$$\left.\begin{aligned}
A_0 &= \Big[\sum_{j=0}^{4} A_{(1,j)} x_0^j\Big] y_0 + \Big[\sum_{j=0}^{4} A_{(3,j)} x_0^j\Big] y_0^3 + \Big[\sum_{j=0}^{4} A_{(5,j)} x_0^j\Big] y_0^5, \\
A_1 &= \sum_{j=0}^{4} A_{(1,j)} x_0^j + 3\Big[\sum_{j=0}^{4} A_{(3,j)} x_0^j\Big] y_0^2 + 5\Big[\sum_{j=0}^{4} A_{(5,j)} x_0^j\Big] y_0^4, \\
A_2 &= 3\Big[\sum_{j=0}^{4} A_{(3,j)} x_0^j\Big] y_0 + 10\Big[\sum_{j=0}^{4} A_{(5,j)} x_0^j\Big] y_0^3, \\
A_3 &= \sum_{j=0}^{4} A_{(3,j)} x_0^j + 10\Big[\sum_{j=0}^{4} A_{(5,j)} x_0^j\Big] y_0^2, \\
A_4 &= 5\Big[\sum_{j=0}^{4} A_{(5,j)} x_0^j\Big] y_0, \\
A_5 &= \sum_{j=0}^{4} A_{(5,j)} x_0^j.
\end{aligned}\right\} \tag{15}$$

The value of $\partial C_{\mathrm{L}}/\partial x_0$ at x_0 can therefore be written as

$$\frac{\partial C_{\mathrm{L}}}{\partial x_0} = \sum_{j=0}^{5} B_j Y^j, \tag{16}$$

$$\left.\begin{aligned}
B_0 &= \Big[\sum_{j=1}^{4} jA_{(1,j)} x_0^{(j-1)}\Big] y_0 + \Big[\sum_{j=1}^{4} jA_{(3,j)} x_0^{(j-1)}\Big] y_0^3 + \Big[\sum_{j=1}^{4} jA_{(5,j)} x_0^{(j-1)}\Big] y_0^5, \\
B_1 &= \sum_{j=1}^{4} jA_{(1,j)} x_0^{(j-1)} + 3\Big[\sum_{j=1}^{4} jA_{(3,j)} x_0^{(j-1)}\Big] y_0^2 + 5\Big[\sum_{j=1}^{4} jA_{(5,j)} x_0^{(j-1)}\Big] y_0^4, \\
B_2 &= 3\Big[\sum_{j=1}^{4} jA_{(3,j)} x_0^{(j-1)}\Big] y_0 + 10\Big[\sum_{j=1}^{4} jA_{(5,j)} x_0^{(j-1)}\Big] y_0^3, \\
B_3 &= \sum_{j=1}^{4} jA_{(3,j)} x_0^{(j-1)} + 10\Big[\sum_{j=1}^{4} jA_{(5,j)} x_0^{(j-1)}\Big] y_0^2, \\
B_4 &= 5\Big[\sum_{j=1}^{4} jA_{(5,j)} x_0^{(j-1)}\Big] y_0, \\
B_5 &= \sum_{j=1}^{4} jA_{(5,j)} x_0^{(j-1)}.
\end{aligned}\right\} \tag{17}$$

In the region of galloping instability, the drag coefficient can similarly be expressed by a polynomial of degrees 3 and 6 in terms of x_0 and y_0+Y respectively. Thus

$$C_D = \sum_{j=0}^{6} C_j Y^j, \tag{18}$$

where

$$\left.\begin{aligned}
C_0 &= \sum_{j=0}^{3} C_{(0,j)} x_0^j + \left[\sum_{j=0}^{3} C_{(2,j)} x_0^j\right] y_0^2 + \left[\sum_{j=0}^{3} C_{(4,j)} x_0^j\right] y_0^4 + \left[\sum_{j=0}^{3} C_{(6,j)} x_0^j\right] y_0^6,\\
C_1 &= 2\left[\sum_{j=0}^{3} C_{(2,j)} x_0^j\right] y_0 + 4\left[\sum_{j=0}^{3} C_{(4,j)} x_0^j\right] y_0^3 + 6\left[\sum_{j=0}^{3} C_{(6,j)} x_0^j\right] y_0^5,\\
C_2 &= \sum_{j=0}^{3} C_{(2,j)} x_0^j + 6\left[\sum_{j=0}^{3} C_{(4,j)} x_0^j\right] y_0^2 + 15\left[\sum_{j=0}^{3} C_{(6,j)} x_0^j\right] y_0^4,\\
C_3 &= 4\left[\sum_{j=0}^{3} C_{(4,j)} x_0^j\right] y_0 + 20\left[\sum_{j=0}^{3} C_{(6,j)} x_0^j\right] y_0^3,\\
C_4 &= \sum_{j=0}^{3} C_{(4,j)} x_0^j + 15\left[\sum_{j=0}^{3} C_{(6,j)} x_0^j\right] y_0^2,\\
C_5 &= 6\left[\sum_{j=0}^{3} C_{(6,j)} x_0^j\right] y_0,\\
C_6 &= \sum_{j=0}^{3} C_{(6,j)} x_0^j.
\end{aligned}\right\} \tag{19}$$

Substitution of C_D, $\partial C_L/\partial x_0$, C_L and $\partial C_L/\partial Y$ from (18), (16) and (14) in (10) results in an equation with constant terms. To free this equation from these terms, the following linear transformation is adopted:

$$Y = z+p, \tag{20}$$

in which z and p represent a new variable and a constant respectively. Upon equating the constant terms to zero, the following relationship is found for the computation of p:

$$p+nU^2 \sum_{j=0}^{5} A_j p^j = 0. \tag{21}$$

Then the differential equation of motion takes the following nonlinear autonomous form:

$$\ddot{z}+\omega_n^2 z = -n\omega_n U f(z,\dot{z}), \tag{22}$$

where $f(z,\dot{z})$ is a lengthy polynomial in terms of z and $\dot{z}$, which is not written here for the sake of brevity. Since the mass parameter is usually small ($n \ll 1$), an approximate periodic solution to (22) can be sought in the form

$$z = a\cos(\omega_n t+\phi), \tag{23}$$

where a is the reduced amplitude defined as vibration amplitude divided by cylinder diameter, and ϕ denotes the phase, both of which are assumed to be slowly varying functions of time t. Applying the first approximation of Krylov & Bogoliubov (1949), the following relationship can be written for the reduced amplitude:

$$\frac{da}{dt} = K_0(a) = \frac{nU}{2\pi}\int_0^{2\pi} f(a\cos\psi,\ -a\omega_n\sin\psi)\sin\psi\,d\psi, \tag{24}$$

in which $\psi = \omega_n t + \phi$. A similar expression can be written for the instantaneous response frequency ω_c:

$$\omega_c^2 = \omega_n^2 + \frac{nU\omega_n}{\pi a}\int_0^{2\pi} f(a\cos\psi, -a\omega_n \sin\psi)\cos\psi \, d\psi. \tag{25}$$

The steady-state amplitude corresponds to $a = a_0$, where a_0 is a constant. The amplitudes of steady vibration are therefore determined by putting (24) equal to zero. This yields the first steady amplitude $a = 0$. The algebraic equation of non-zero limit-cycle galloping amplitudes is

$$\begin{aligned}
&\sum_{j=0}^{6} C_j p^j - x_0 \sum_{j=0}^{4} (j+1) A_{(j+1)} p^j + (p+y_0) \sum_{j=0}^{5} B_j p^j + \frac{2\beta}{nU} \\
&+\left[\sum_{j=0}^{4} \tfrac{1}{4}(j+1) B_{(j+1)} p^j\right] a + [\tfrac{1}{4}C_2 - \tfrac{3}{4}x_0 A_3 + \tfrac{1}{4}B_2 y_0 + (\tfrac{3}{4}C_3 - 3x_0 A_4 + \tfrac{1}{4}B_2 + \tfrac{3}{4}B_3 y_0) p \\
&+ \tfrac{3}{2}(C_4 - 5x_0 A_5 + \tfrac{1}{2}B_3 + B_4 y_0) p^2 + \tfrac{1}{2}(5C_5 + 3B_4 + 5B_5 y_0) p^3 + \tfrac{5}{2}(\tfrac{3}{2}C_6 + B_5) p^4] a^2 \\
&+ (\tfrac{1}{8}B_3 + \tfrac{1}{2}B_4 p + \tfrac{5}{4}B_5 p^2) a^3 + \tfrac{1}{8}[C_4 - 5x_0 A_5 + B_4 y_0 + (5C_5 + B_4 + 5B_5 y_0) p \\
&+ 5(3C_6 + B_5) p^2] a^4 + \tfrac{5}{64}B_5 a^5 + \tfrac{5}{64}C_6 a^6 = 0.
\end{aligned} \tag{26}$$

The steady-state vibration-frequency ratio $\Omega = \omega_c/\omega_n$ can similarly be computed from the following relationship:

$$\Omega^2 = 1 + nU^2\left[\sum_{j=0}^{4} (j+1) A_{(j+1)} p^j + 3(\tfrac{1}{4}A_3 + A_4 p + \tfrac{5}{2}A_5 p^2) a^2 + \tfrac{5}{8}A_5 a^4\right]. \tag{27}$$

Also of interest is the critical flow speed for the initiation of galloping U_0. This is obtained by putting $a = 0$ in (26). Using a phase-plane approach (the plane of $\dot{a}$ against a), it may easily be concluded that the amplitude $a = a_0$ is stable if

$$\left[\frac{dK_0(a)}{da}\right]_{a=a_0} < 0, \tag{28}$$

in which $K_0(a)$ is defined by (24). It is unstable otherwise. The condition for self-excitation from the mean position is

$$\left[\frac{d\dot{a}}{da}\right]_{a=a_0-0} = \left[\frac{dK_0(a)}{da}\right]_{a=a_0} > 0. \tag{29}$$

3. Experimental set-up and programme

The investigation was conducted in a rectangular horizontal flume 0.3 m wide, 0.3 m high and 18 m long with vertical glass sidewalls. The working section was situated at a distance of about 1 m from the leading streamlined plates of the flume. The water depth at this section was kept constant at roughly 290 mm. A miniature current flowmeter was used for time-mean velocity measurements. The velocity fluctuations were detected by means of a hot-film probe, the output of which was fed into a minicomputer.

The velocity distribution at the test station was sensibly constant over a major portion of the section, with the boundary layer being less than 6 mm. The background turbulence at this section had an intensity $(\overline{v^2})^{\frac{1}{2}}/V = 6.5\,\%$, where v denotes the streamwise fluctuating velocity, and a scale of 16 mm. Free-stream turbulence of high intensity could be generated at the working section by the installation of a turbulence

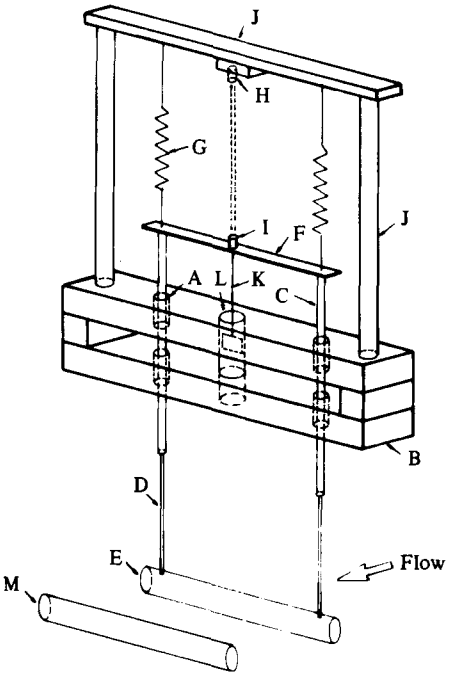

FIGURE 2. Schematic diagram of the dynamic test apparatus: A, air bearing; B, air-bearing housing; C, air-bearing shaft; D, arm; E, vibrating cylinder; F, cross-bar; G, helical spring; H, receiving transducer; I, transmitting transducer; J, rigid frame; K, damper connecting shaft; L, oil pot; M, stationary cylinder.

grid at the distance of 360 mm upstream of this section. This flow had intensity and scale of 11.9% and 8 mm respectively.

A schematic representation of the equipment for dynamic testing is given in figure 2. The vibrating system was suspended from a rigid frame by means of two identical helical springs, each with a stiffness of 8.53 N/m. Using air-bearing devices, the movement of the oscillating upstream cylinder was restricted to a plane normal to the incident flow. The end-clearances between the model and the side walls were 1 mm. The downstream cylinder was held horizontally in the flume, parallel to the rear one. With the aid of a mechanical device, the rear body was able to traverse in either the transverse or streamwise directions. There was practically no end gap between the downstream model and the sidewalls. An ultrasonic displacement-measuring device was used to detect the system movement. External damping could be applied to the system artificially by means of a very thin plate immersed in an oil pot. The mass of the system could be changed by putting additive masses on the cross-bar.

A circular cylinder, with a similar body submerged in its wake, suffers not only from an expected drag force but also a lift force. To measure the static forces on a cylinder as influenced by the proximity to a parallel downstream body, the two cylinders were held vertically with the upstream cylinder always being held in the channel centre plane, as shown in figure 3. The downstream body was strain-gauged at the top. The signal from the straingauge was fed into the minicomputer. Further details of the experimental set-up and the measuring techniques are given elsewhere (Bokaian & Geoola 1984*c*).

The models used comprised two pairs of circular cylinders of 8 and 16 mm diameter.

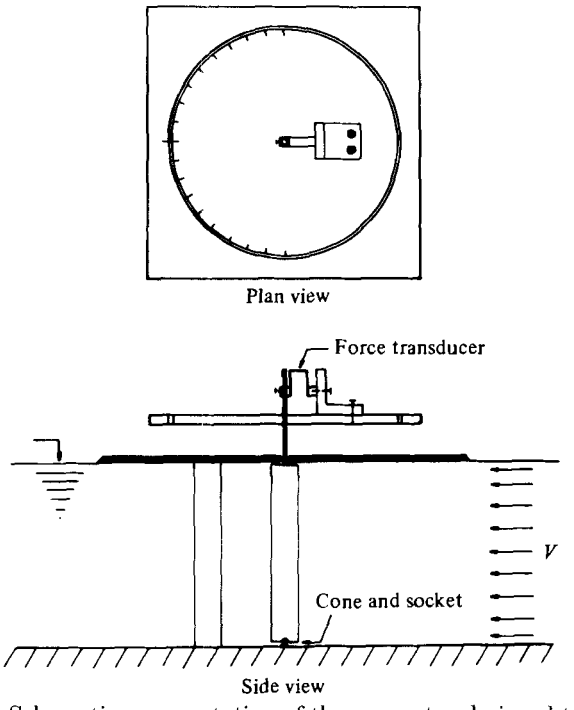

FIGURE 3. Schematic representation of the apparatus designed to measure drag and lift forces on the upstream cylinder.

The cylinders were made of PVC and had a smooth surface. The experiments carried out with the pair of identical cylinders can be broadly classified into two series of static and dynamic tests. In the static experiments the mean fluid-dynamic forces on the upstream cylinder were measured, whereas in the dynamic tests the cross-flow instabilities of the front body were investigated. The two test series covered both arrangements of tandem and staggered relative to the free-stream flow, with longitudinal and transverse separation ranging from 1 to 5 and 0 to 3 diameters respectively. The effects of free-stream turbulence on static forces and also on the fluid-elastic instabilities of the upstream cylinder in the dynamic experiments were to be determined. Using the formula given by Kiya *et al.* (1982), it was found that the cylinder flow (isolated) was within the subcritical regime in all tests. A single cylinder of 16 mm diameter occupied about 5 % of the area of the channel working section. However, no correction was made to the results of this work for the blockage effects.

4. Presentation and analysis of results

4.1. *Vortex-shedding frequency of the upstream cylinder*

A principal characteristic of vortex shedding is the non-dimensional Strouhal number $S_1 = f_s D/V$, where f_s is the shedding frequency of the upstream cylinder. The variation of S_1 (for two stationary cylinders) is shown in figure 4 as a function of spacing ratio x_0 and y_0. These data were taken from the previous work of the authors (Bokaian & Geoola 1984*b*). The most noticeable feature of these data is that, in tandem arrangement, for spacings less than two diameters, the downstream body inhibited the formation of a vortex street on the gap side.

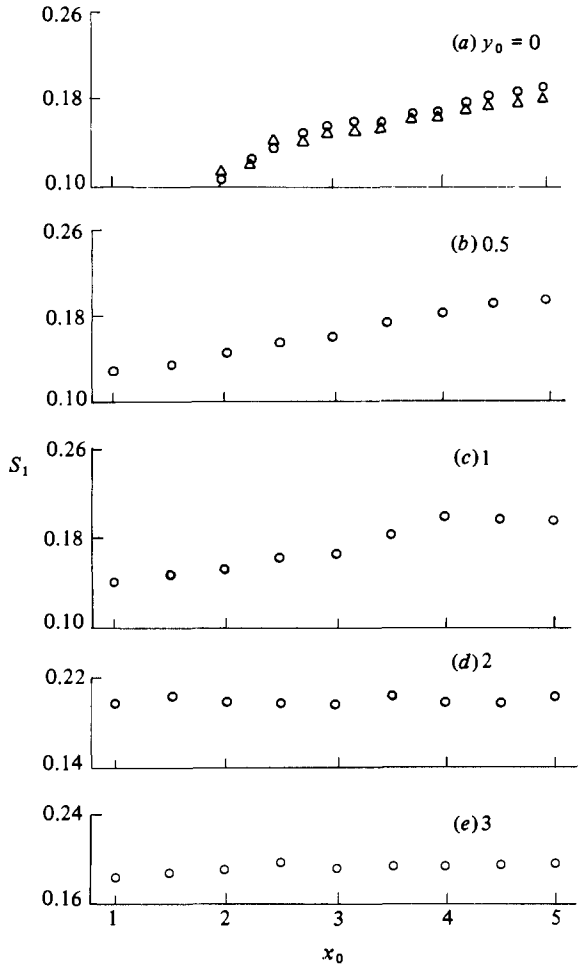

FIGURE 4. Variation of the Strouhal number of the upstream cylinder (fixed) as a function of relative streamwise and transverse spacing (Bokaian & Geoola 1984*b*); $L = 300$ mm, $D = 16$ mm, $(\overline{v^2})^{\frac{1}{2}}/V = 6.5\%$; ○, $Re = 5.6 \times 10^3$; △, $Re = 1.15 \times 10^3$.

4.2. *Static lift and drag coefficients*

Information about the static forces on a circular cylinder upstream of an identical parallel neighbour is rather scarce. Wardlaw & Cooper (1973) seem to be the only researchers who carried out some limited force measurements. A detailed survey of lift and drag forces was made at five longitudinal stations with separations of 1.09, 1.25, 1.5, 1.75 and 2 diameters. At each streamwise station the forces were explored for roughly 22 transverse locations in one side of the flume centreplane (positive lateral spacing). In order to establish the degree of symmetry of drag data and antisymmetry of lift data with respect to the wake centreline, some force measurements were made in the other side of the flume centreplane (negative lateral spacing). At each location the force measurement was repeated at least twice and the average value was taken. The lift and drag forces were converted to their respective lift and drag coefficients using the expressions

$$C_L = (\text{lift force})/(\tfrac{1}{2}\rho DLV^2) \quad \text{and} \quad C_D = (\text{drag force})/(\tfrac{1}{2}\rho DLV^2).$$

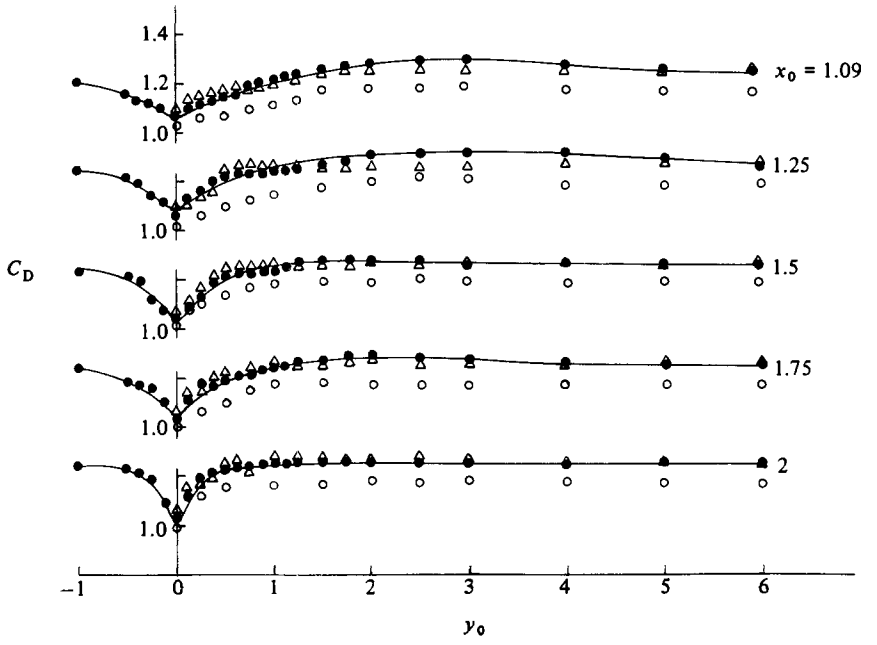

FIGURE 5. Variation of the drag coefficient as a function of longitudinal and lateral spacing ratio: ●, $Re = 5900$, $(\overline{v^2})^{\frac{1}{2}}/V = 6.5\%$; △, 2600, 6.5%; ○, 5900, 11.9%.

The static forces were measured at two Reynolds numbers of 5900 and 2600. In the tests associated with the higher Reynolds number, the measurements were conducted under the two conditions of free-stream turbulence. At the above Reynolds numbers, the drag coefficient $C_{D\infty}$ of a single cylinder showed the respective values of 1.25 and 1.26 in a water flow with 6.5% turbulence intensity, and 1.17 and 1.19 in a flow with turbulence level of 11.9%.

Figure 5 shows the experimental data of drag coefficient as a function of lateral position of the downstream cylinder in the wake of the upstream one. In order that the data be distinguishable from one another, a smooth curve was drawn through the data points associated with the higher Reynolds number $Re = 5900$ under 6.5% turbulence level (note that these curves were not drawn by polynomial fitting). The above figure clearly indicates that the drag force data are symmetrical with respect to the wake centreline. In general, the data tend to be of the same form, a typical example of which over half of the wake is indicated in figure 6. In this figure the drag coefficient denotes a minimum value C_{D0} when the two cylinders are in tandem arrangement; the minimum drag value always being less than the single-cylinder value.

Figure 6 reveals that, in general, on increasing the transverse separation, the drag coefficient increases continuously from the point of minimum on the wake centreline and attains the free-stream value at a relatively small lateral spacing. From this, it may be inferred that in the near wake the drag forces were lower than the single-cylinder values. With further increases in transverse separation, the steady increase in the magnitude of the drag coefficient continues until a peak is reached. This peak probably corresponds to a position fairly close to the edge of the wake. Beyond this point the drag force slowly decreases, approaching the free-stream value at a very large lateral spacing.

Figure 5 shows that the drag-force data are still very much in evidence when the

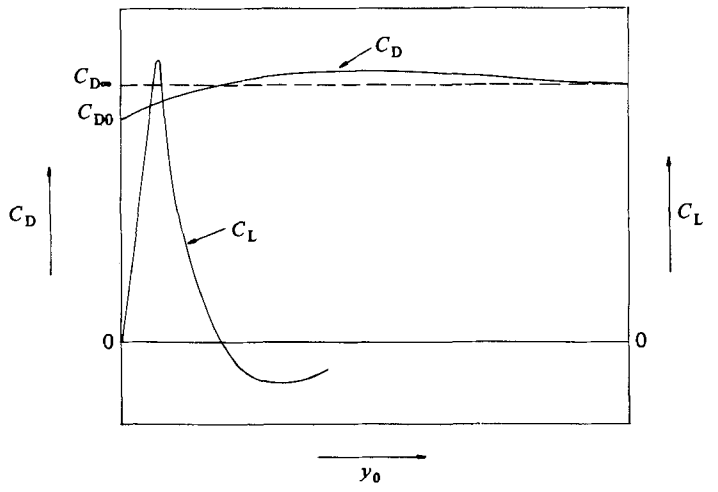

FIGURE 6. General representation of the variation of lift and drag coefficients as a function of lateral position in the wake.

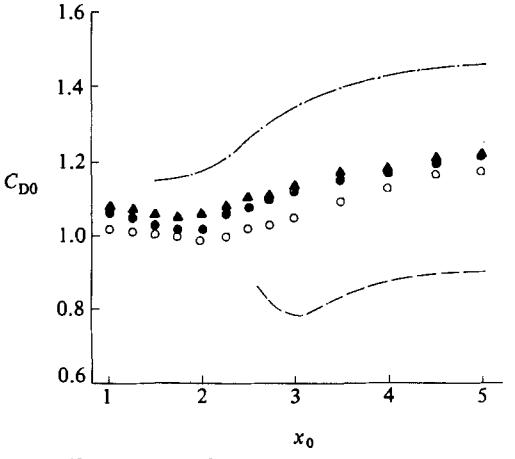

FIGURE 7. Variation of drag coefficient in tandem arrangement aganst the longitudinal spacing ratio. Present study: ●, Re = 5900, $(\overline{v^2})^{\frac{1}{2}}/V$ = 6.5 %; ▲, 2600, 6.5 %; ○, 5900, 11.9 %. Tanida *et al.* (1973): – – –, 3400, 0.1 %. Kostic & Oka (1972): –·–·–·–, 13000, 2.8 %.

two cylinders are placed at 2 diameters streamwise separation. Moreover it indicates that the drag coefficient changes only slightly with a limited change in Reynolds number from 2600 to 5900. In contrast, the effect of turbulence on the lateral variation of drag force can be seen to be profound and becomes quite noticeable at a sufficiently small transverse spacing; this probably being due to free-stream drag variation. As the above figure clearly denotes, an increase in turbulence intensity from 6.5 % to 11.9 % do not destroy the profiles, but it generally tends to lower the value of drag coefficient and smoothens the drag data.

The measured data of minimum drag coefficient C_{D0} versus x_0 are indicated in figure 7. Also plotted in this figure are the data obtained by previous workers having Reynolds numbers near to those of the present study. They comprise the observations of Tanida, Okajima & Watanabe (1973) obtained by towing two cylinders in a water tank at a Reynolds number Re = 3400, and those of Kostic & Oka (1972) calculated from the circumferential pressure distribution in a uniform turbulent flow of a wind tunnel with an intensity of 2.8 % at Re = 13000.

Despite the fact that in tandem arrangement the vortex-shedding process behind the upstream body takes place for spacings greater than two diameters, the drag data of this study indicate no discontinuity in relation to the cylinders' separation. Figure 7 shows that there exist considerable differences between the data points of various workers. Similar differences exist between the results of other investigators which are not plotted in the above figure. Whilst the experimental techniques used to obtain the drag force (strain gauge, pressure distribution etc.) and the errors involved could in part be responsible for so much difference between the results of various workers, it may generally be concluded that the Reynolds number, turbulence characteristics and the cylinders' aspect ratio, collectively or individually, are governing factors in the variation of drag coefficient versus the spacing.

The measured values of the lift coefficient C_L as a function of relative spacing x_0 and y_0 are similarly represented in figure 8. In drawing this figure the positive direction of the lift force was assumed to be towards the downstream cylinder's streamwise axis. A smooth curve was again drawn through the data points with 6.5 % turbulence intensity at higher Reynolds number $Re = 5900$. This figure clearly demonstrates that the lift forces were approximately zero when the two cylinders were aligned longitudinally. The lift-coefficient data all look antisymmetrical with respect to the wake centreline. A typical lateral variation of the lift force over half of the wake is shown in figure 6. It is clear from figure 8 that the lift force field is essentially unaffected by a limited increase in Reynolds number or turbulence intensity. However, it must be mentioned that Wardlaw & Cooper (1973) observed some variation in the value of static coefficients with changing Reynolds number.

As the lift data indicate, for a fixed and small longitudinal separation, as the downstream cylinder is moved from the free stream to the wake centreline, the lift force on the front body increases until it reaches a peak at a relatively small lateral spacing. Figure 9 shows the sketch of the flow patterns at this peak, obtained by injecting potassium permanganate into the wake. It is clear from this figure that the downstream cylinder significantly alters the near-wake structure of the upstream one, and in doing so squeezes the streamlines between the two bodies. The two rows of vortices from the adjacent sides interlock, resulting in a complex flow pattern behind the cylinder pair. It is not surprising that a comparison of the lateral variation of the lift force on the front body at small separations (figure 8) and the corresponding one on the rear cylinder, as reported by Bokaian & Geoola (1983*c*), clearly shows that both peak at exactly the same transverse position.

The measured maximum lift coefficient $C_{L\max}$ and the corresponding relative lateral spacing $y_{\max}$ versus the longitudinal separation ratio x_0 are plotted in figure 10. Lift coefficients as large as nearly 0.8 can be seen. This figure clearly shows that, at two diameters' spacing, the lift force on the front cylinder becomes almost negligible. Furthermore it indicates that the interaction effects and the resulting lift force on the upstream body sharply increases as the downstream cylinder goes inside the wake of the upstream one.

4.3. *Dynamic-test results*

The assembly for dynamic testing was adjusted so that the cylinder position in still water was halfway between the flume bed and the water surface. A series of 35 dynamic experiments was undertaken, the important details of which can be found in table 1. Columns (1), (2) and (3) represent the run number and the corresponding relative separations x_0 and y_0 respectively. The natural circular frequency of the system in still water ω_n, and hence the total vibrating mass m, and also the viscous damping coefficient c, were obtained by plucking excitation in still water. The initial

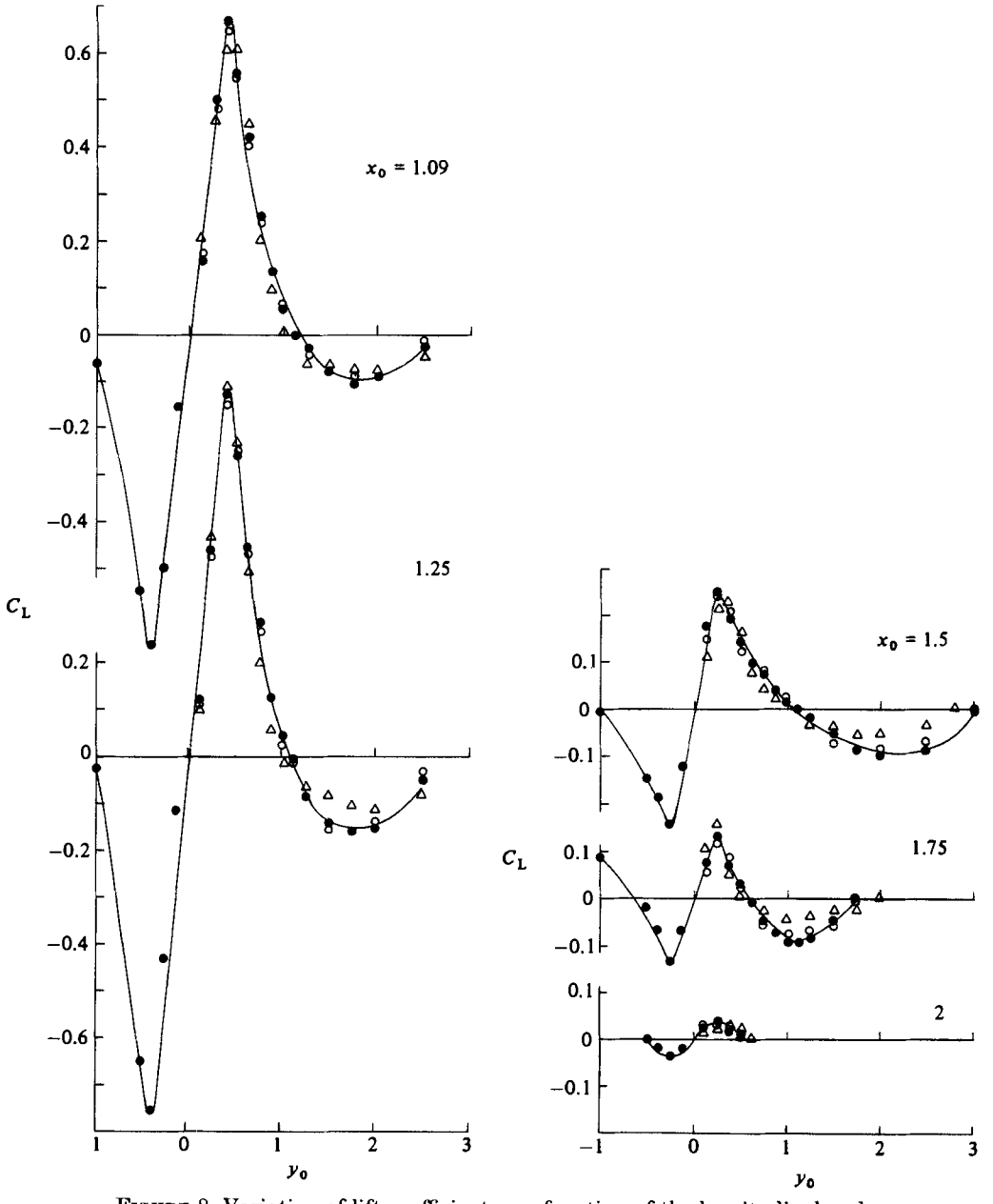

FIGURE 8. Variation of lift coefficient as a function of the longitudinal and lateral spacing ratio. Symbols as in figure 5.

displacement to the system relative to the equilibrium position Y_0 was about 50 mm. Columns (4), (5), (6), (7) and (8) give the values of the ω_n, the vibratory Reynolds number $\gamma = \omega_n D^2/\nu$, the added-mass coefficient C_M, the reduced damping $\beta = c/2m\omega_n$ and the mass parameter $n = \rho D^2 L/2m$ of the experiments respectively. C_M was calculated by dividing the measured still water added mass by $\frac{1}{4}\rho\pi LD^2$. In each dynamic test, the values of the natural circular frequency ω_n, the reduced damping β and the mass parameter n of the vibrating system were fixed. Measurements of the free-stream velocity V in the flume, together with a simultaneous recording

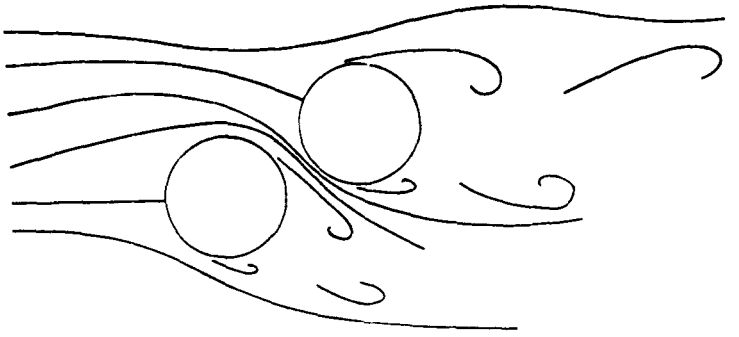

FIGURE 9. Sketch of flow patterns at the maximum lift force.

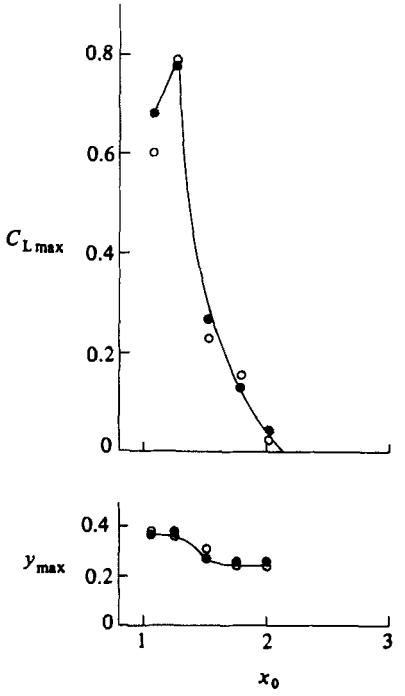

FIGURE 10. Variation of the maximum lift coefficient and the corresponding lateral spacing ratio as functions of relative longitudinal separation: ●, $Re = 5900$, $(\overline{v^2})^{\frac{1}{2}}/V = 6.5\,\%$; ○, $Re = 2600$, $(\overline{v^2})^{\frac{1}{2}}/V = 6.5\,\%$.

of the oscillation amplitude and frequency, were made. Column (11) shows the approximate Reynolds-number range of the tests.

Indicated in column (9) of table 1 are the values of the vortex-resonance speed $U_r = 1/2\pi S_1$, where S_1 is the Strouhal number of the vortex-shedding behind the upstream body (see figure 4). The bar in this column denotes the lack of vortex-shedding at the corresponding spacing. Column (10) shows the values of stability parameter $k_s = 2\pi\beta/n$.

Figures 11–16 summarize the dynamic test data in a dimensionless form with the reduced amplitude a and the oscillation-frequency ratio $\Omega = \omega_c/\omega_n$ plotted against the reduced flow velocity $U = V/(\omega_n D)$. The small vertical arrows on the U-axis indicate the vortex-resonance speed U_r. The reduced velocity was varied between

Run number (1)	Longitudinal-spacing ratio x_0 (2)	Lateral-spacing ratio y_0 (3)	Natural circular frequency ω_n (rad/s) (4)	Vibratory Reynolds number $\gamma = \frac{\omega_n D^2}{\nu}$ ($\nu = 10^{-6}$ m^2/s) (5)	Added-mass coefficient C_M (6)	Reduced damping $\beta = \frac{c}{2m\omega_n}$ (7)	Mass parameter $n = \frac{\rho D^2 L}{2m}$ ($\rho = 10^3$ kg/m^3) (8)	Vortex-resonance speed $U_r = \frac{1}{2\pi S_1}$ (9)	Stability parameter $k_s = \frac{2\pi\beta}{n}$ (10)	Reynolds-number range $Re = \frac{VD}{\nu}$ ($\nu = 10^{-6}$ m^2/s) (11)
T1†	1.09	0.00	4.16	1065	1.68	0.0113	0.0774	—	0.917	1400–5950
T2*a*†	1.25	0.00	4.16	1065	1.68	0.0113	0.0774	—	0.917	1150–5950
T2*b*†‖	1.25	0.00	4.10	1050	1.68	0.0410	0.0751	—	3.430	1600–5850
T2*c*‡	1.25	0.00	4.52	289	2.13	0.0419	0.0375	—	7.020	650–2100
T2*d*†	1.25	0.00	4.10	1050	1.69	0.0891	0.0751	—	7.454	2800–5750
T2*e*†	1.25	0.00	4.10	1050	1.68	0.1257	0.0751	—	10.517	3650–5650
T3†	1.50	0.00	4.16	1065	1.67	0.0113	0.0774	—	0.917	1150–5950
T4†	1.75	0.00	4.16	1065	1.67	0.0113	0.0774	—	0.917	800–5950
T5†	2.00	0.00	4.16	1065	1.67	0.0113	0.0774	1.49	0.917	800–2100
T6†	3.00	0.00	4.16	1065	1.70	0.0113	0.0772	1.02	0.920	800–2100
T7†	4.00	0.00	4.16	1065	1.70	0.0113	0.0772	0.95	0.920	800–1600
T8†	5.00	0.00	4.16	1065	1.70	0.0113	0.0772	0.83	0.920	800–1600
P1†	1.09	0.50	4.16	1065	1.67	0.0117	0.0774	1.23	0.950	1100–6000
P2†	1.25	0.50	4.16	1065	1.67	0.0117	0.0774	1.21	0.950	1300–6000
P3†	1.50	0.50	4.16	1065	1.68	0.0117	0.0774	1.19	0.950	800–2100
P4†	1.75	0.50	4.16	1065	1.68	0.0117	0.0774	1.13	0.950	750–2100
P5†	2.00	0.50	4.16	1065	1.68	0.0117	0.0774	1.08	0.950	750–1950
P6†	3.00	0.50	4.16	1065	1.69	0.0117	0.0774	1.00	0.950	750–1950
P7†	4.00	0.50	4.16	1065	1.69	0.0117	0.0774	0.87	0.950	700–1800
P8†	5.00	0.50	4.16	1065	1.70	0.0117	0.0772	0.82	0.952	700–1700

Q1†	1.09	1.00	4.16	1065	1.67	0.0118	0.0774	1.13	0.958	950–1700
Q2†	2.00	1.00	4.16	1065	1.68	0.0118	0.0774	1.05	0.958	800–1700
Q3†	3.00	1.00	4.16	1065	1.68	0.0118	0.0774	0.95	0.958	800–1700
Q4†	4.00	1.00	4.16	1065	1.68	0.0118	0.0774	0.80	0.958	650–1700
Q5†	5.00	1.00	4.16	1065	1.67	0.0118	0.0774	0.82	0.958	650–1700
R1†	1.09	2.00	4.16	1065	1.69	0.0114	0.0774	0.80	0.925	650–1350
R2†	2.00	2.00	4.16	1065	1.69	0.0114	0.0774	0.80	0.925	650–1600
R3†	3.00	2.00	4.16	1065	1.69	0.0114	0.0774	0.80	0.925	650–1950
R4†	4.00	2.00	4.16	1065	1.70	0.0114	0.0772	0.80	0.928	650–1950
R5†	5.00	2.00	4.16	1065	1.70	0.0114	0.0772	0.79	0.928	650–1950
S1†	1.09	3.00	4.16	1065	1.70	0.0114	0.0772	0.86	0.928	650–1600
S2†	2.00	3.00	4.16	1065	1.70	0.0114	0.0772	0.83	0.928	650–1800
S3†	3.00	3.00	4.16	1065	1.70	0.0114	0.0772	0.83	0.928	800–1800
S4†	4.00	3.00	4.16	1065	1.68	0.0114	0.0774	0.81	0.925	800–1750
S5†	5.00	3.00	4.16	1065	1.68	0.0114	0.0774	0.81	0.925	800–1750

† Cylinder made of PVC; cylinder diameter $D = 16$ mm; cylinder length $L = 298$ mm; cylinder aspect ratio $L/D = 18.63$; initial-displacement ratio $\eta = Y_0/D = 3.13$.

‡ Cylinder made of dural; cylinder diameter $D = 8$ mm; cylinder length $L = 298$ mm; cylinder aspect ratio $L/D = 37.25$; initial-displacement ratio $\eta = Y_0/D = 6.25$.

‖ Wake observations behind the vibrating cylinder.

TABLE 1. Significant details of the dynamic experiments

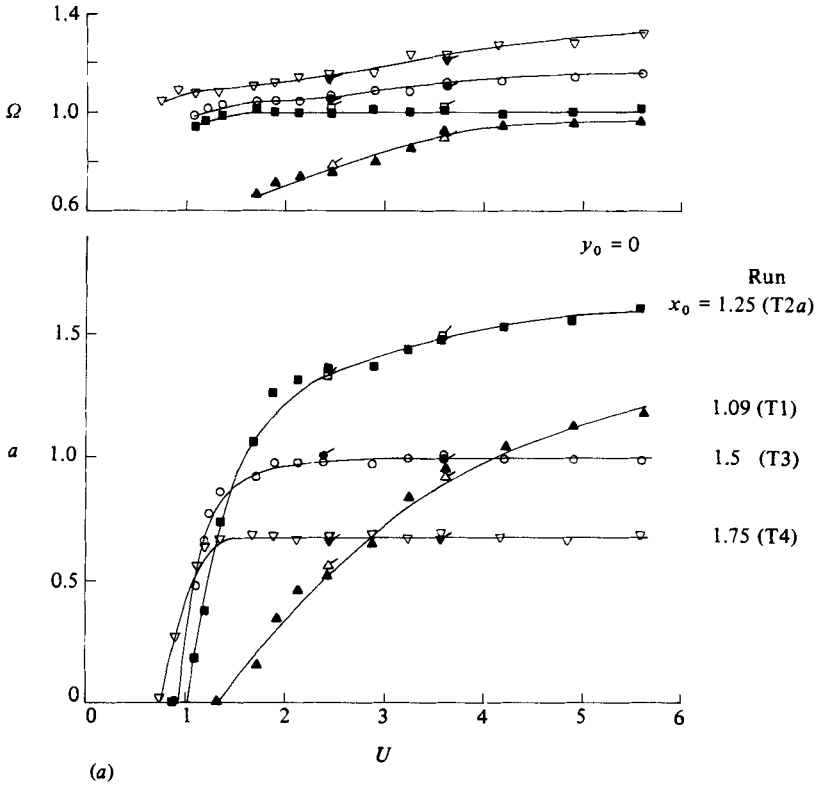

FIGURE 11 (*a*). For caption see facing page.

approximately 0 and 6, usually by changing V and holding the values of ω_n and D constant. In some runs, the mean position of the upstream cylinder, either when the body was oscillating or stationary, varied with changing free-stream flow speed. The data associated with the variation of the dimensionless mean position p versus the reduced velocity are also plotted in the above figures. No appreciable change in the results can be seen with changing the turbulence intensity from 6.5% to 11.9%.

In the dynamic results two kinds of instability, namely a vortex-resonance and galloping, can be seen. Indicated in the lower part of figure 17 is the type of instability that was observed at each separation. 'a' refers to a vortex lock-in, while 'b' denotes a galloping instability. As can be deduced from this figure, the type of excitation observed depends entirely on the cylinders' spacing. The essential element for the occurrence of galloping instability is the location of the downstream body in a critical region of the wake of the upstream one. Motions will then commence above some threshold flow speed. The galloping vibrations only occur when the rear cylinder is well inside the near wake of the front one.

The tests plotted in figures 11–15 all have approximately the same value of stability parameter, between 0.917 and 0.958. The experimental data of tandem arrangement are shown in the first figure. The runs T1, T2*a*, T3 and T4, drawn in figure 11 (*a*), which have small separations of 1.09, 1.25, 1.5 and 1.75 diameters respectively, all indicate a galloping instability. The most noticeable feature of the data with small spacings is that, on increasing the flow velocity, the wake-induced forces cause a slow and steady rise of the vibration frequency; the oscillation becoming generally faster.

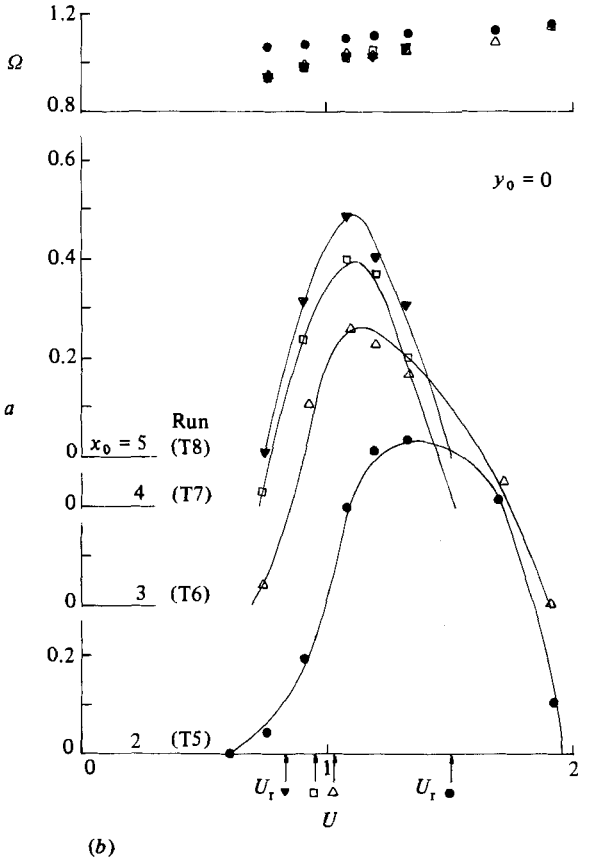

FIGURE 11. Variation of the reduced amplitude and the oscillation-frequency ratio against the reduced velocity in tandem arrangement. (*a*) ▲, △, run T1; ■, □, T2*a*; ○, ●, T3; ▽, ▼, T4 (the first symbol represents the 6.5 % turbulence intensity, while the second one denotes the 11.9 % turbulence level). (*b*) ●, T5; △, T6; □, T7; ▼, T8. ($(\overline{v^2})^{\frac{1}{2}}/V = 6.5\,\%$).

For the smallest gap between the two bodies ($x_0 = 1.09$), the vibration began at a reduced velocity of about $U_0 = 1.3$. The oscillation amplitude denotes a progressive but slow increase with increasing flow velocity. It seems that the vibration amplitudes reach a limit value at a reduced velocity considerably higher than 6. The oscillation-frequency data at $x_0 = 1.09$ show similarly a continual increase with an increase in flow velocity. The vibration frequency had a value of $\omega_c \approx 0.65\omega_n$ at the instability onset, and attained a value of $\omega_c \approx 0.95\omega_n$ at the reduced velocity of $U \approx 4.5$. It remained at this value thereafter.

With an increase in the separation to 1.25 diameters, the value of the critical reduced velocity for galloping dropped to $U_0 \approx 1$. The oscillation amplitudes and frequencies at this position, particularly in the reduced-velocity range $U \lesssim 4$, were considerably larger than the corresponding ones at $x_0 = 1.09$. It is interesting to remember that the magnitude of the static lift forces at the position $x_0 = 1.25$ were also larger than those at $x_0 = 1.09$ (see figure 8). However, at 1.25 diameters spacing, the vibration amplitudes appear to reach a limit value at a reduced velocity of about 6. The oscillation-frequency data do not show any significant variation in relation to flow velocity; the value of ω_c being slightly less than ω_n.

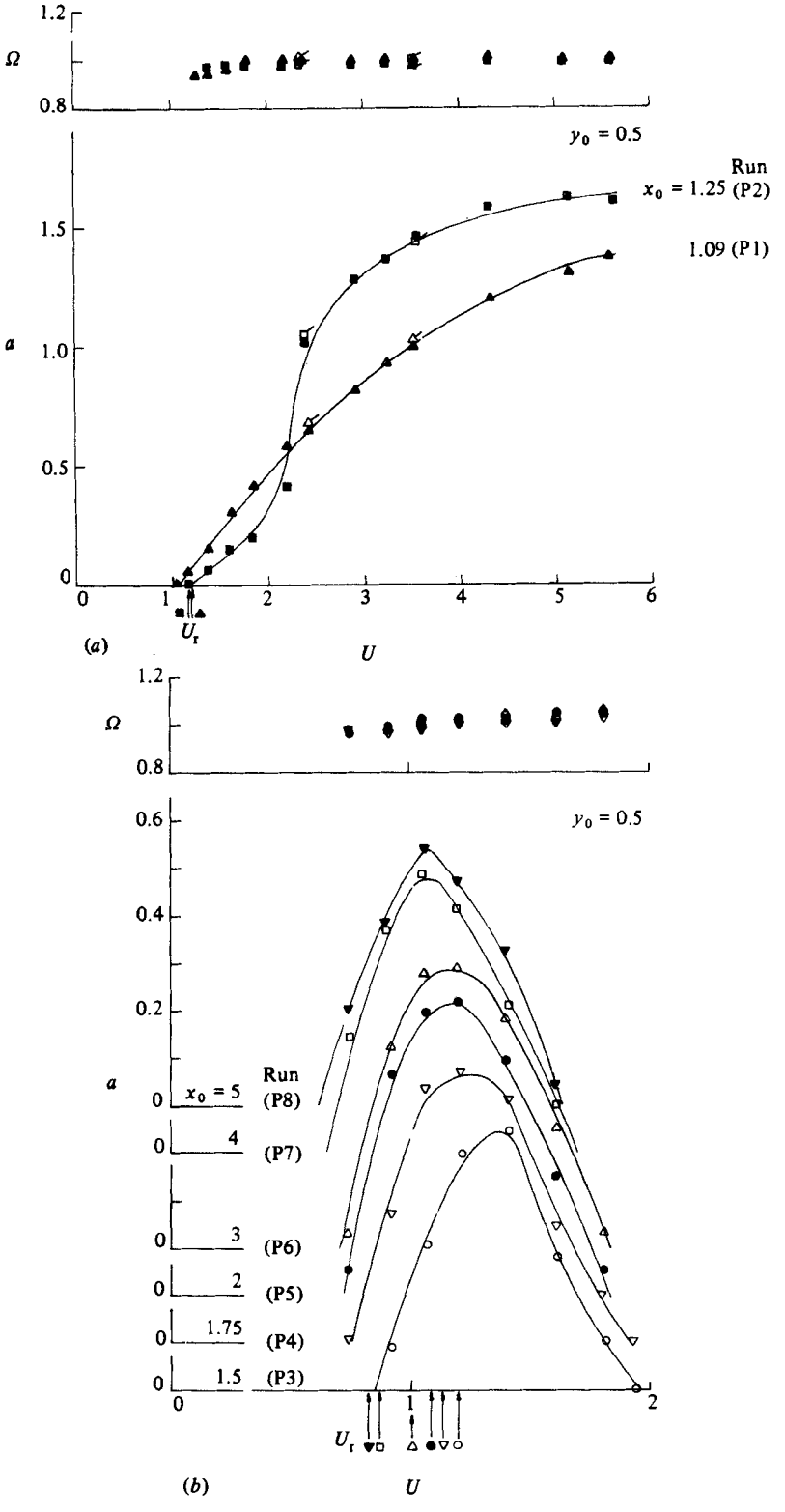

FIGURE 12 (*a*, *b*). For caption see facing page.

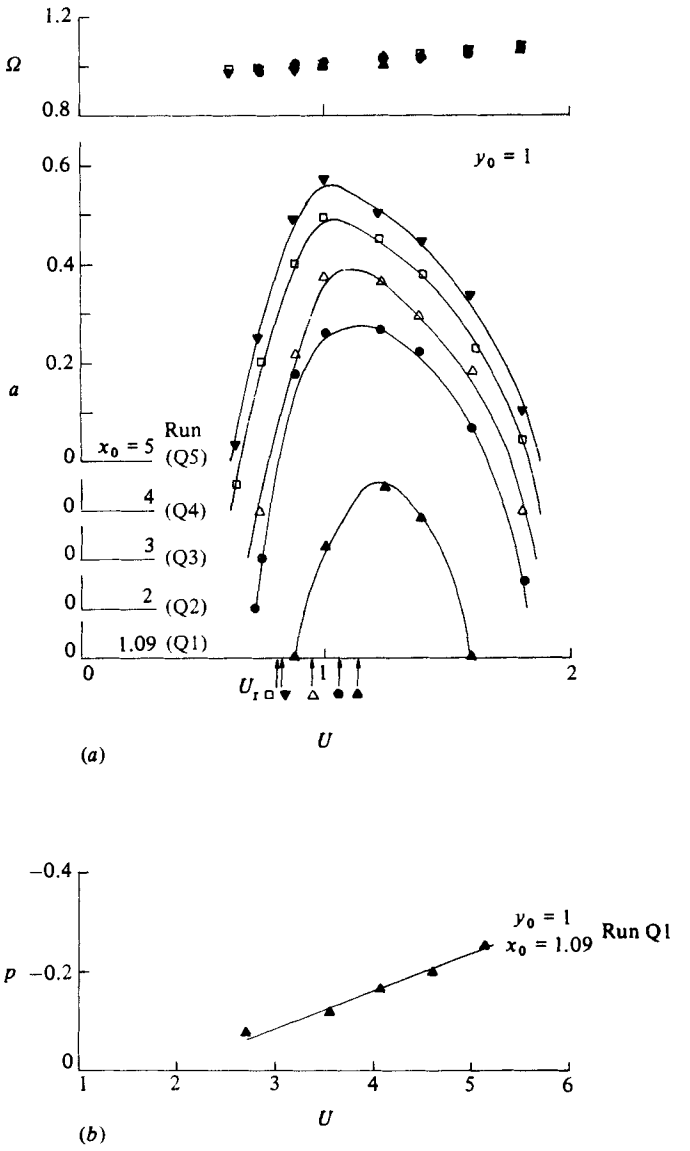

FIGURE 13. Variation of the reduced amplitude, the oscillation frequency ratio, and the cylinder mean position against the reduced velocoty in staggered arrangement. ▲, run Q1; ●, Q2; △, Q3; □, Q4; ▼, Q5. $(\overline{v^2})^{\frac{1}{2}}/V = 6.5\,\%$.

FIGURE 12. Variation of the reduced amplitude and the oscillation frequency ratio against the reduced velocity in staggered arrangement. (*a*) ▲, △, run P1; ■, □, P2 (the first symbol represents the 6.5 % turbulence intensity, while the second one denotes the 11.9 % turbulence level). (*b*) ○, P3; ▽, P4; ●, P5; △, P6; □, P7; ▼, P8. $(\overline{v^2})^{\frac{1}{2}}/V = 6.5\,\%$.

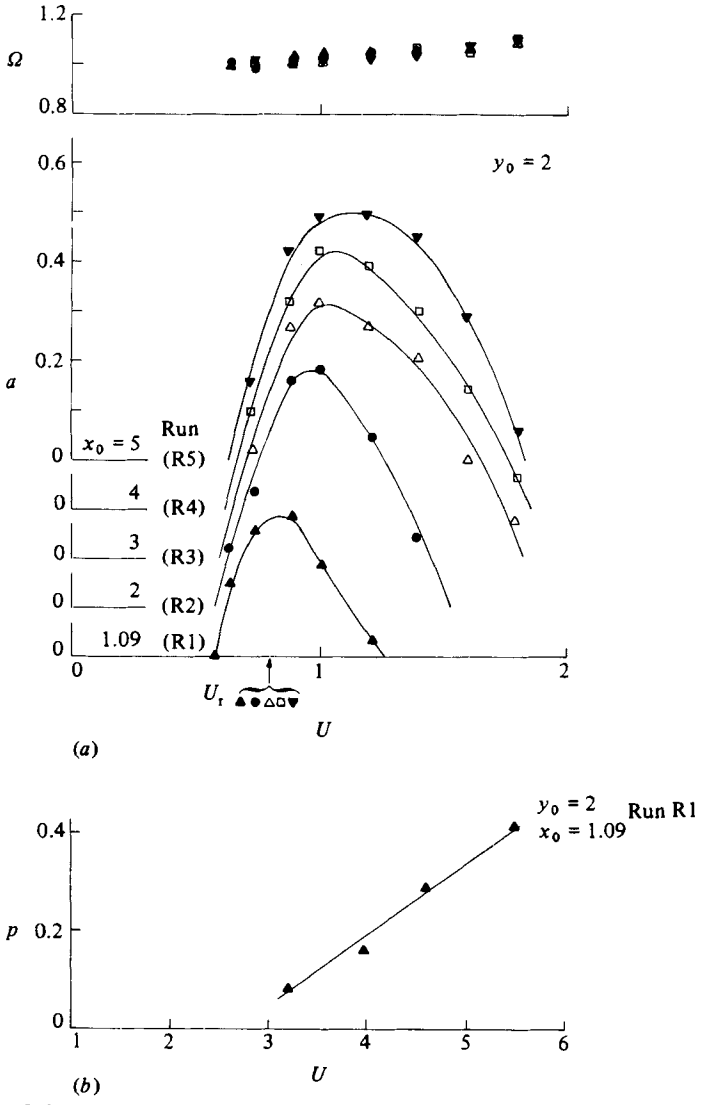

FIGURE 14. Variation of the reduced amplitude, the oscillation-frequency ratio, and the cylinder mean position against the reduced velocity in staggered arrangement. ▲, run R1; ●, R2; △, R3; □, R4; ▼, R5. $(\overline{v^2})^{\frac{1}{2}}/V = 6.5\%$.

Further increases in the separation from 1.25 to 1.5 and 1.75 diameters caused the value of U_0 to decrease from 1 to 0.9 and 0.75 respectively. The reduced-amplitude profiles at positions $x_0 = 1.25$, 1.5 and 1.75 are similar to one another, but are very different from that at $x_0 = 1.09$. At these stations, the vibration amplitude rapidly increases with increasing flow speed until a certain amplitude is reached. Beyond this, the rate of increase declines considerably, with the oscillation amplitude quickly approaching a constant value. The variation of the vibration-frequency ratio versus the reduced velocity at separations $x_0 = 1.5$ and 1.75 has the same pattern, and indicates a slow increase with an increase in the flow speed, even when the oscillation amplitude remains at a constant value.

From the above observations, it may be deduced that in tandem arrangement, on

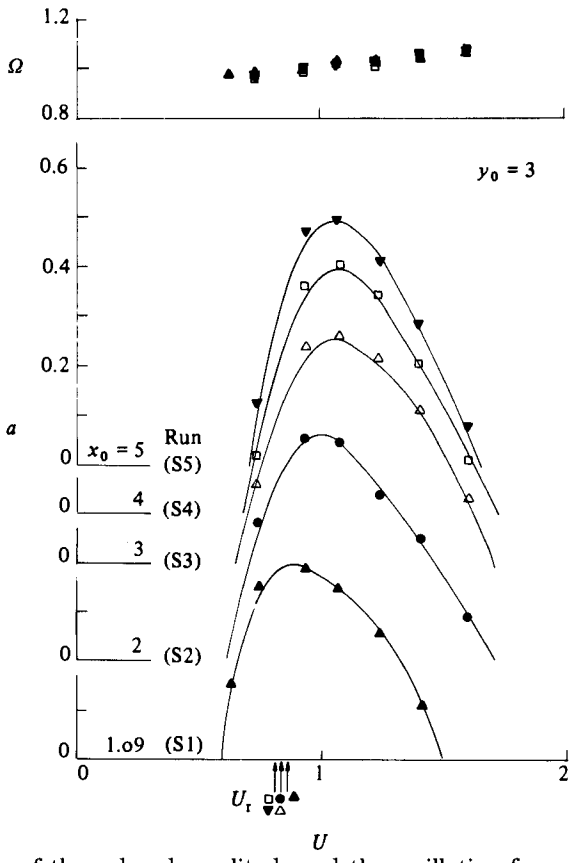

FIGURE 15. Variation of the reduced amplitude and the oscillation frequency ratio against the reduced velocity in staggered arrangement. ▲, run S1; ●, S2; △, S3; □, S4; ▼, S5. $(\overline{v^2})^{\frac{1}{2}}/V = 6.5\,\%$.

increasing the gap between the pair of cylinders, the galloping instability begins at a smaller flow velocity, the vibration amplitude attains a limit value at a smaller flow speed, the limit oscillation amplitude generally decreases, and the vibration becomes generally faster. All these are only true if the gap always remains sufficiently small. From what has been described so far, it is evident that the behaviour of proximity-induced galloping, both in amplitude and frequency domains, is essentially different from that of galloping of isolated non-circular cylinders, in which the oscillation frequency remains at a constant value, and, at sufficiently high values of reduced velocity, the vibration amplitude varies almost linearly in relation to flow speed (Blevins 1977).

As can be seen in figure 11 (*b*), the data points at stations with spacings 2, 3, 4 and 5 diameters, corresponding to tests T5, T6, T7 and T8 respectively, all indicate a vortex-excited resonance. The reduced-amplitude profiles are similar amongst themselves. As this figure clearly shows, the reduced velocity range of lock-in, the peak resonance amplitude, the corresponding reduced velocity, and the vortex-resonance speed all decrease on increasing the gap. At each station, some difference can be seen between the reduced velocity at the maximum lock-in amplitude and the corresponding vortex-resonance speed. It is interesting to note that at two diameters position the peak resonance amplitude is roughly equal to the limit galloping amplitude at $x_0 = 1.75$ (run T4), but is about half of that at $x_0 = 1.25$ (run T2*a*).

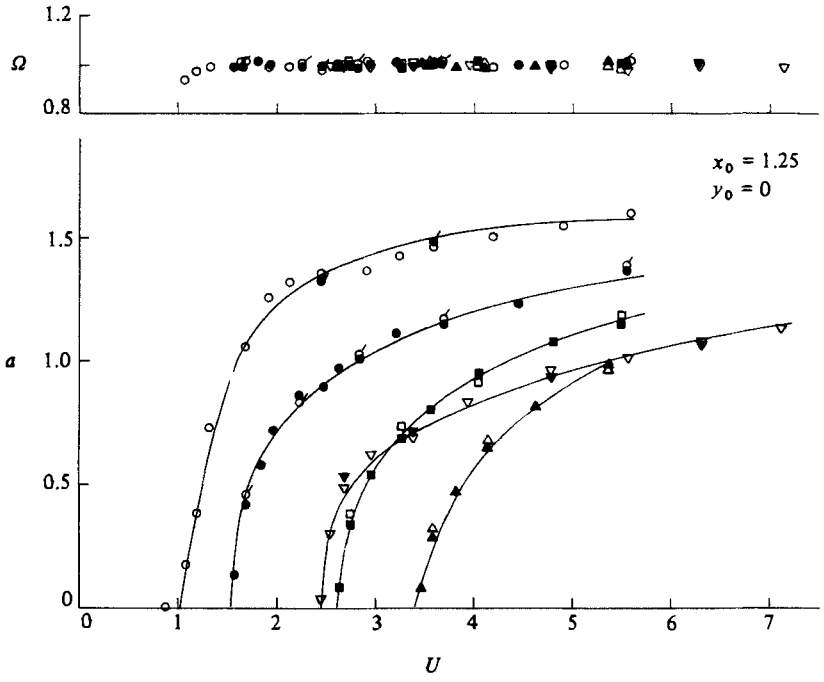

FIGURE 16. Variation of the reduced amplitude and the oscillation frequency ratio against the reduced velocity in tandem arrangement at different stability parameter levels. ○, ◐, run T2*a*; ●, ◑, T2*b*; ▽, ▼, T2*c*; ■, □, T2*d*; ▲, △, T2*e* (the first symbol represents the 6.5% turbulence intensity, while the second one denotes the 11.9% turbulence level).

Furthermore, at $x_0 = 2$, the vibration began with a frequency slightly higher than the natural frequency of the system, and indicated a slow increase when the flow speed was increased. The oscillation frequency data at positions $x_0 = 3$, 4 and 5 collapse onto one another and lie somewhat below those of $x_0 = 2$. They clearly denote that the cylinder oscillated with frequencies differing only marginally from their still-water values.

The dynamic test observations of staggered arrangement with transverse separation of 0.5 cylinder diameters are shown in figure 12. In these experiments, the cylinder mean position indicated no appreciable variation in relation to flow velocity. The galloping vibration data are plotted in figure 12(*a*). The reduced-amplitude profiles at spacings $x_0 = 1.09$ (test P1) and $x_0 = 1.25$ (test P2) are rather similar to the corresponding ones in tandem arrangement (runs T1 and T2*a* respectively). The limit oscillation amplitude at $x_0 = 1.25$ in both staggered and tandem arrangements appears to be about the same. However, in the staggered arrangement, an increase in the streamwise gap from 1.09 to 1.25 diameters caused a small increase in the reduced velocity U_0 for galloping onset. It may be surprising that at position $x_0 = 1.25$ the value of U_0 indicates a good agreement with the corresponding vortex-resonance speed U_r, while at $x_0 = 1.09$ the value of U_0 differs but little from the corresponding value of U_r. The vibration-frequency data at both separations fall onto one another. The instability began with a frequency slightly less than the system's natural frequency, but for reduced velocities greater than 1.8 they locked to one another. This behaviour is different from those observed in tandem arrangement. Figure 17 denotes that no galloping vibration occurred for spacings greater than $x_0 = 1.25$ and $y_0 = 0.5$.

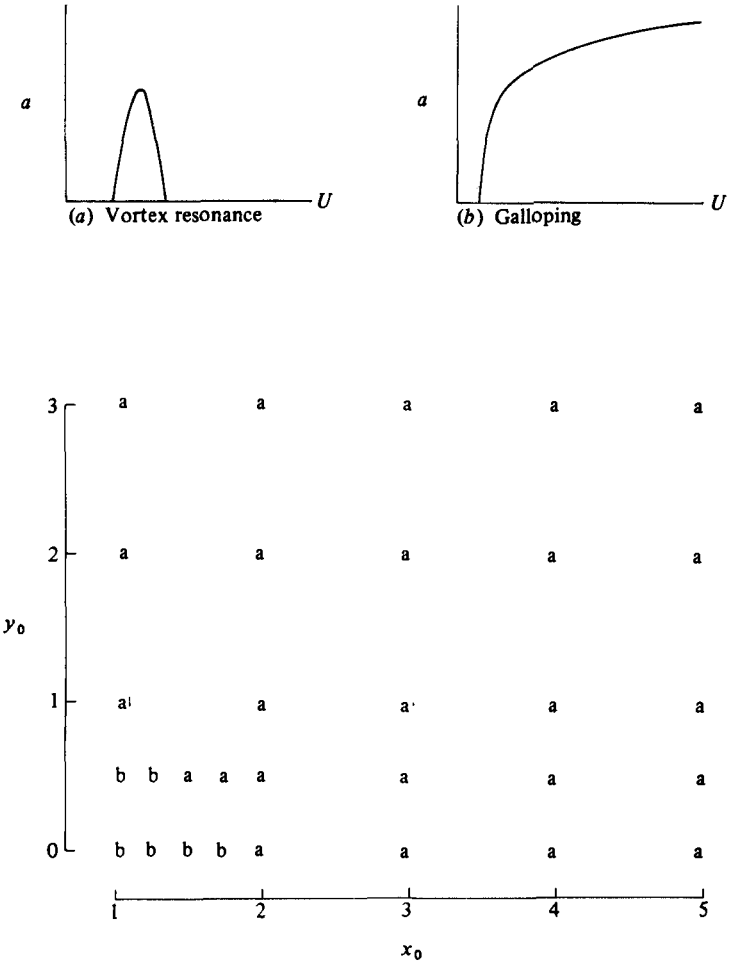

FIGURE 17. Variation of the reduced amplitude against the reduced velocity at various cylinders separations.

A number of important conclusions may be drawn from the dynamic-test data examined so far. First, the galloping amplitudes and frequencies remain essentially unaffected by a limited increase in free-stream turbulence intensity. Secondly, for flow velocities greater than a critical value, galloping oscillations build up from an equilibrium position (cylinder position in still water). These two characteristics of proximity-induced galloping are in contrast with those of isolated sharp-edged bodies, in which, depending on the cross-sectional geometry, turbulence can have profound effects on the cylinder behaviour, and some initial displacement (triggering amplitude) may be required to excite the cylinder to gallop (Blevins 1977). Thirdly, the extent of the galloping instability depends on the cylinders' relative position. An increase in the flow velocity does not extend the area of instability further downstream. Galloping instability only occurs when the rear cylinder is well inside the near wake of the front one.

The measured results of tests P3, P4, P5, P6, P7 and P8, which have separations of 1.5, 1.75, 2, 3, 4 and 5 diameters respectively, all show a vortex-induced oscillation. As figure 12(*b*) clearly indicates, the vibration began with a frequency slightly less

than the natural frequency ω_n of the system. The oscillation frequency ω_c showed a steady but very slow increase with increasing flow speed. At the end of the vortex-resonance excitation, the value of ω_c was only slightly higher than that of ω_n. When the streamwise gap was increased, the reduced velocity range of lock-in, the shape and the value of peak resonance amplitude remained roughly the same. However, the reduced velocity at the maximum lock-in amplitude, and the vortex-resonance speed generally decreased with increasing the longitudinal gap. This behaviour is similar to that observed in tandem arrangement (see figure 11*b*).

The dynamic-test data of staggered arrangement with transverse spacings of 1, 2 and 3 diameters are similarly plotted in figures 13, 14 and 15 respectively. Only a vortex-excited resonance can be seen in these figures. At a given lateral separation, the reduced velocity range of vortex lock-in, and the peak resonance amplitude generally increase with increasing the streamwise gap. However, whilst at the transverse spacing ratio of $y_0 = 1$ (see figure 13*a*), the reduced velocity at peak resonance amplitude generally decreases when x_0 is increased (similar to the trend observed at $y_0 = 0$ and 0.5 in figures 11*b*, 12*b*), there exists an opposite behaviour at $y_0 = 2$ and 3 in figures 14(*a*) and 15. An interesting point is that for the smallest streamwise gap ($x_0 = 1.09$) and at lateral separation of one diameter (run Q1), at high flow velocities outside the vortex-resonance range where the cylinder was almost stationary, the cylinder mean position varied almost linearly with flow speed. With an increase in the lateral separation to two diameters (test R1 with $x_0 = 1.09$ and $y_0 = 2$), a similar behaviour was observed, but with the difference that the direction of cylinder displacement was opposite to that of run Q1. No such phenomena occurred at $y_0 = 3$. In staggered arrangement, again at each station, some difference can be seen between the reduced velocity at peak lock-in amplitude and the corresponding vortex-resonance speed. From a comparison of all the vibration frequency data, it may be deduced that in staggered arrangement the variation of the oscillation-frequency ratio Ω with reduced velocity U is essentially independent of the cylinders' spacing.

The effects of changing the cylinders' aspect ratio on the behaviour of proximity-induced galloping can be examined by comparing the experimental observations of runs T2*c* and T2*d*, as shown in figure 16. The two tests have significantly different aspect ratios but possess the same separation, and were designed to have roughly the same value of stability parameter. This figure quite clearly indicates that an increase in the aspect ratio from $L/D = 18.63$ to 37.25 caused some differences in the oscillation amplitudes, though the vibration frequencies remained essentially unchanged. From this it may be inferred that galloping amplitudes are sensitive to the cylinders' aspect ratio. This characteristic of proximity-induced galloping is similar to that of galloping of a single sharp-edged body.

Changing the structural damping can have significant effects on the cross-flow instabilities of isolated bluff bodies (Wawzonek & Parkinson 1979; Bokaian & Geoola 1984*a*). The effects of changing the structural damping on the behaviour of proximity-excited galloping is examined by comparing the results of tests T2*a*, T2*b*, T2*d* and T2*e*, as shown in figure 16. In these experiments the cylinder pair was in tandem arrangement and had a gap of 0.25 diameters. This spacing was deliberately chosen since the oscillation amplitudes were the greatest (see figure 11*a*). The above runs display a number of interesting features. First, as is to be expected, on increasing the structural damping, the vibration amplitudes generally decrease and a higher flow velocity is needed to excite the cylinder to gallop. Secondly, in general, the oscillation frequency locked to the system natural frequency in spite of considerable changes

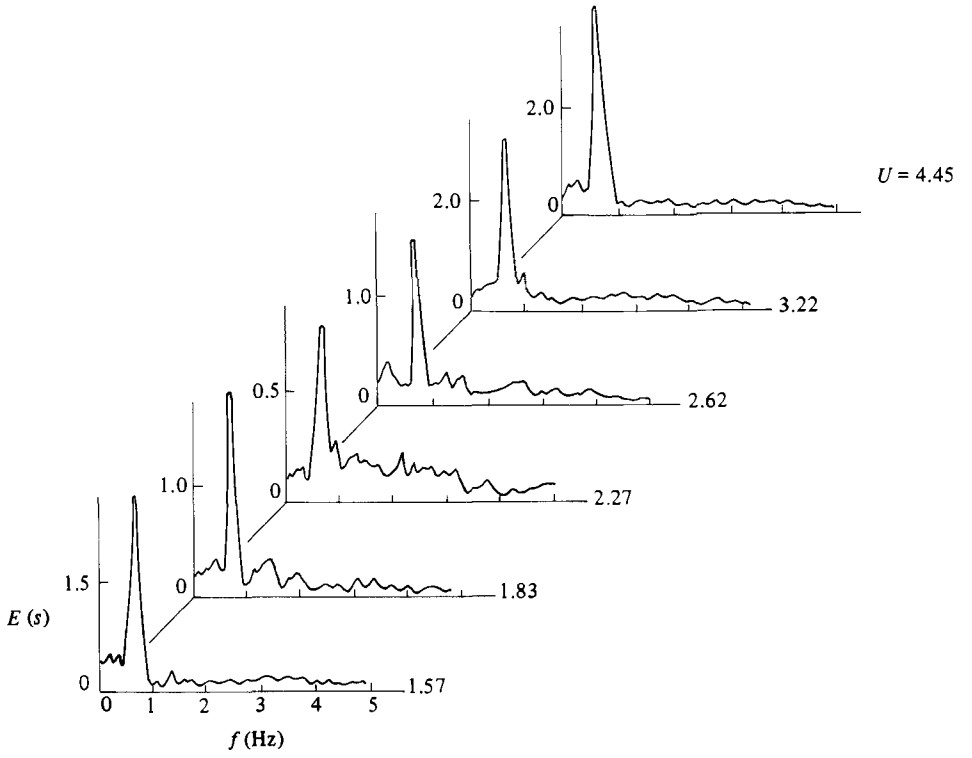

FIGURE 18. Normalized spectral-density plots of wake fluctuations behind the galloping cylinder in test T2*b*.

in flow speed and structural damping. Thirdly, although the abovementioned tests have significantly different values of stability parameter k_s, nevertheless the variation of the reduced amplitude versus reduced velocity at all four levels of k_s is similar. This characteristic of proximity-induced galloping is in sharp contrast to that of galloping instability of isolated non-circular cylinders.

4.4. *Wake fluctuations behind the vibrating cylinder*

As described in §4.1, for a pair of stationary identical cylinders in tandem arrangement, up to two diameters spacing, the downstream body inhibited the vortex formation behind the upstream one. However, visualization of flow patterns by injecting potassium permanganate into the front cylinder's wake indicated that, when this body is allowed to vibrate, a vortex-shedding process always takes place behind it. In test T2*b* the wake fluctuations were measured behind the galloping cylinder at various flow speeds. The gap between the cylinder pair was 0.25 diameters. The hot-film probe was positioned in the centreplane of the flume, just outside the near wake of the vibrating body. Figure 18 represents typical examples of the power spectra of the fluctuating velocity in the wake, with E and f denoting the normalized spectral-density function and the shedding frequency respectively. Indicated on the right-hand side of each figure is the corresponding reduced flow velocity. All the spectra have a single clear and sharp peak at a predominant frequency. This is an evidence that the wake velocity was fluctuating in a fairly sinusoidal manner, and hence the presence of a strong vortex-shedding process.

Figure 19 summarizes the variation of the dimensionless vortex-shedding frequency

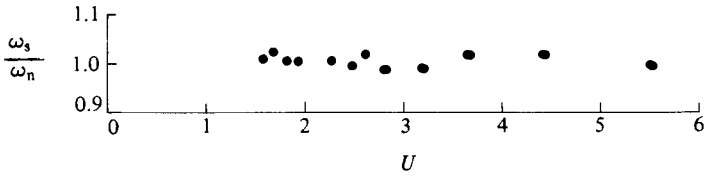

FIGURE 19. Variation of the dimensionless vortex-shedding frequency of the galloping cylinder against the reduced velocity in test T2*b*.

ω_s/ω_n, where ω_s is the circular vortex-shedding frequency as estimated from the peak in the power spectrum, against the reduced velocity. This figure clearly denotes that the values of the data points ω_s/ω_n do not deviate appreciably from 1. It should be remembered that in run T2*b* the vibration frequency was approximately equal to the system's natural frequency (see figure 16). Observations of wake patterns indicated that the cylinder shed regularly a pair of strong vortices during one oscillation cycle, irrespective of a change in the free-stream velocity. These findings conclusively demonstrate that during galloping motion the vortex-shedding frequency locked to the vibration frequency. This behaviour of proximity-excited galloping is puzzling, because it is similar to that of a vortex resonance rather than galloping instability of isolated cylinders. During galloping vibration of a bluff body, the shedding frequency varies linearly in relation to flow speed, (Bokaian & Geoola 1984*a*).

4.5. *Prediction of galloping amplitude and frequency*

As can be seen in figure 17, within the range of spacings, Reynolds numbers and other governing parameters tested, the galloping instability occurs when the separation ratio x_0 and y_0 falls within a trapezoid with vertices at ($x_0 = 1.09$, $y_0 = 0$), ($x_0 = 1.09$, $y_0 = 0.5$), ($x_0 = 1.75$, $y_0 = 0$) and ($x_0 = 1.25$, $y_0 = 0.5$). Considering that during large-amplitude galloping motion the cylinder can go outside this boundary, a larger area in the form of a rectangle with vertices at ($x_0 = 1.09$, $y_0 = 0$), ($x_0 = 1.09$, $y_0 = 1.5$), ($x_0 = 2.0$, $y_0 = 0$) and ($x_0 = 2.0$, $y_0 = 1.5$) was defined for the purpose of surface fitting. This boundary covers the entire area that may be occupied by the galloping cylinder. To approximate the variation of lift and drag coefficients in terms of the cylinders' spacing, the method of least squares was employed, orthogonal polynomials being used (Hayes 1970).

Using the measured drag data in 6.5% turbulence intensity (figure 5) and the lift data (figure 8), it was found that the variation of lift and drag coefficients could satisfactorily be approximated by (14) and (18) respectively. The constant coefficients of the surfaces are given in tables 2 and 3.

An attempt was made to compare the measured galloping data with the corresponding computed ones as predicted by the quasi-steady approach. This was done by replotting the results of the dynamic tests T1 and T2*a* of figure 11, and T2*b*, T2*d* and T2*e* of figure 16 in a similar manner in figure 20. Superimposed on these graphs are the corresponding theoretical galloping curves. They are based on the relationships (26) and (27), the data of table 1 and the coefficients given in tables 2 and 3. The full lines represent the stable limit-cycle galloping oscillations, while the broken lines denote the unstable ones, as verified by (28). In runs T2*a*, T2*b*, T2*d* and T2*e*, the coexistence of stable and unstable vibrations for a given reduced velocity is an indication that (26) has two real positive roots. In tests T2*a* and T2*b* (figures 20*b*, *c*), the stable and unstable solutions have different amplitudes but possess equal frequencies.

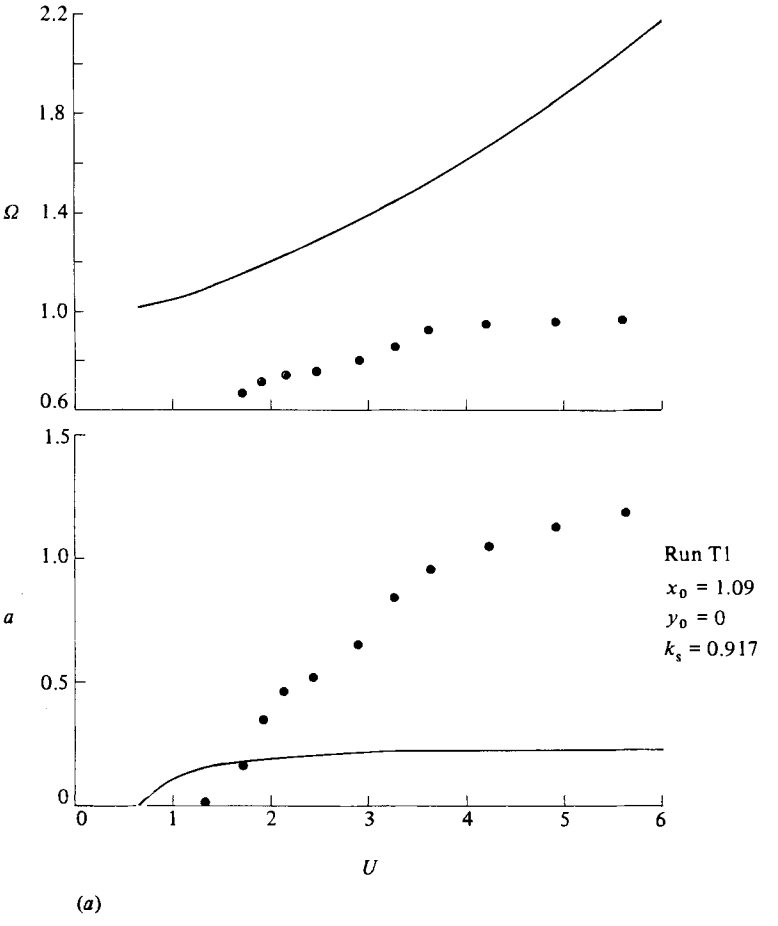

(*a*)

FIGURE 20(*a*). For caption see p. 448.

$A_{(1,0)}$	−201.06530	$A_{(3,0)}$	295.98285	$A_{(5,0)}$	−87.89065
$A_{(1,1)}$	544.68433	$A_{(3,1)}$	−807.38568	$A_{(5,1)}$	240.64642
$A_{(1,2)}$	−536.66174	$A_{(3,2)}$	802.85098	$A_{(5,2)}$	−240.31059
$A_{(1,3)}$	229.74973	$A_{(3,3)}$	−347.38023	$A_{(5,3)}$	104.45051
$A_{(1,4)}$	−36.22640	$A_{(3,4)}$	55.39871	$A_{(5,4)}$	−16.73430

TABLE 2. Coefficients of polynomial approximation of the variation of lift coefficient

$C_{(0,0)}$	−0.64385	$C_{(2,0)}$	−3.17987	$C_{(4,0)}$	5.66581
$C_{(0,1)}$	3.54489	$C_{(2,1)}$	7.02447	$C_{(4,1)}$	−12.01435
$C_{(0,2)}$	−2.33990	$C_{(2,2)}$	−4.66194	$C_{(4,2)}$	8.01931
$C_{(0,3)}$	0.50511	$C_{(2,3)}$	1.01839	$C_{(4,3)}$	−1.75411
		$C_{(6,0)}$	−1.72233		
		$C_{(6,1)}$	3.62699		
		$C_{(6,2)}$	−2.41967		
		$C_{(6,3)}$	0.52848		

TABLE 3. Coefficients of polynomial approximation of the variation of drag coefficient

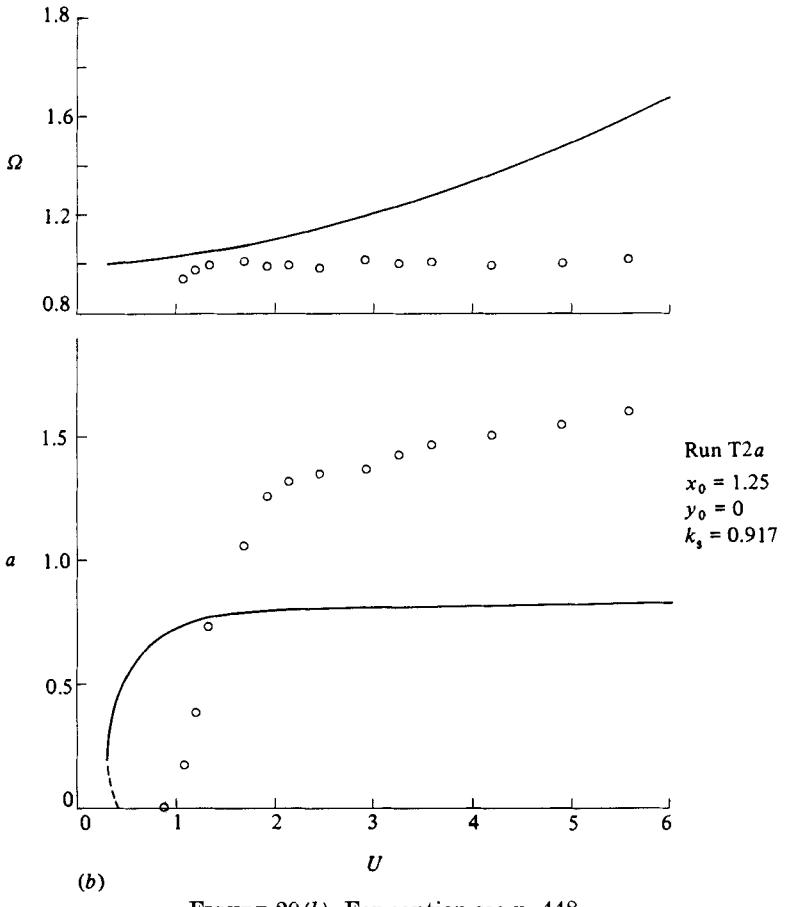

FIGURE 20(*b*). For caption see p. 448.

As can be seen in figure 20, in the amplitude domain both the predicted and the measured responses show a trend of increase as the flow speed is increased; the vibration amplitudes approaching limit values asymptotically. A comparison of the results of tests T2*a*, T2*b*, T2*d* and T2*e* reveals that, as the structural damping is increased, the predicted value of the reduced velocity for galloping onset increases, and the computed vibration amplitudes generally decrease. These two trends are consistent with those of the measured data. Notice that, in tests other than T1, the theory predicts that some triggering amplitude is required in order to excite the cylinder to gallop. This behaviour is contrary to that of observed results. It seems that the computer predictions are sensitive to the polynomial approximation of the static forces. If more thorough static-force data had been available, this kind of error might have been lessened, and better predictions would have been achieved.

It is difficult to explain the reason behind the differences between the measured values and the computed ones in the abovementioned tests. It is possible that the cylinder added mass in the streaming flow deviated from the corresponding still-fluid value. However, even if there was any such deviation, it would probably be small enough to explain the large differences in frequency domain. Another possible reason is that the quasi-steady theory takes into account only the galloping forces, and not the forces induced by the vortex-shedding process. It is possible that in proximity-excited galloping the forces due to the shed vortices play a significant role. If the

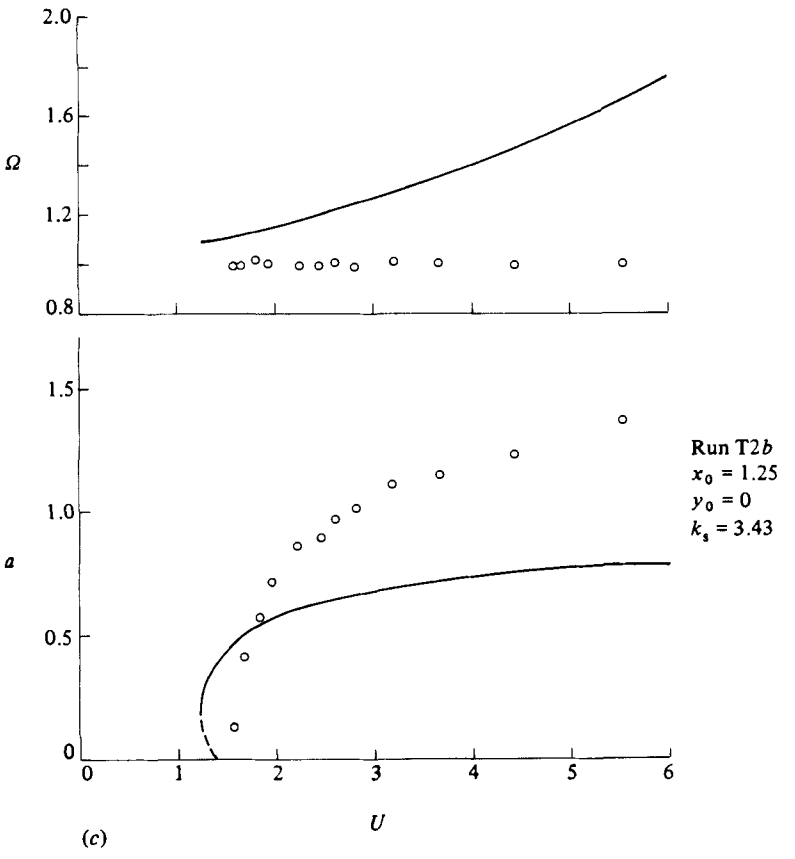

(*c*)

FIGURE 20(*c*). For caption see p. 448.

fluctuating lift and drag forces on the upstream member of a stationary cylinder pair were known, one would have an idea of the order of magnitude of these forces as compared with galloping forces.

5. Summary and conclusions

The flow around a stationary or vibrating smooth circular cylinder, as influenced by the proximity to a fixed identical downstream body, displayed a number of interesting characteristics. In the static experiments, the variation of lift and drag coefficients was found to be antisymmetrical and symmetrical with respect to the wake centreline respectively; the minimum drag force being on this line. In the near wake the lift forces attained peak values while the drag forces remained lower than single-cylinder values. An increase in turbulence intensity lowered the drag-coefficient value, and smoothed the drag data, but had no appreciable effect on the lift data. The forces on the front cylinder differed from those on an isolated body only if the two cylinders were as close as three diameters. It was generally concluded that the free-stream Reynolds number, turbulence characteristics and cylinders' aspect ratio, collectively or individually, are significant factors in the static tests.

The dynamic experiments, carried out over the reduced-velocity range of 0–6, indicated either a vortex lock-in or a galloping instability. The latter always builds up from an equilibrium position, and only occurs when the rear body is well inside

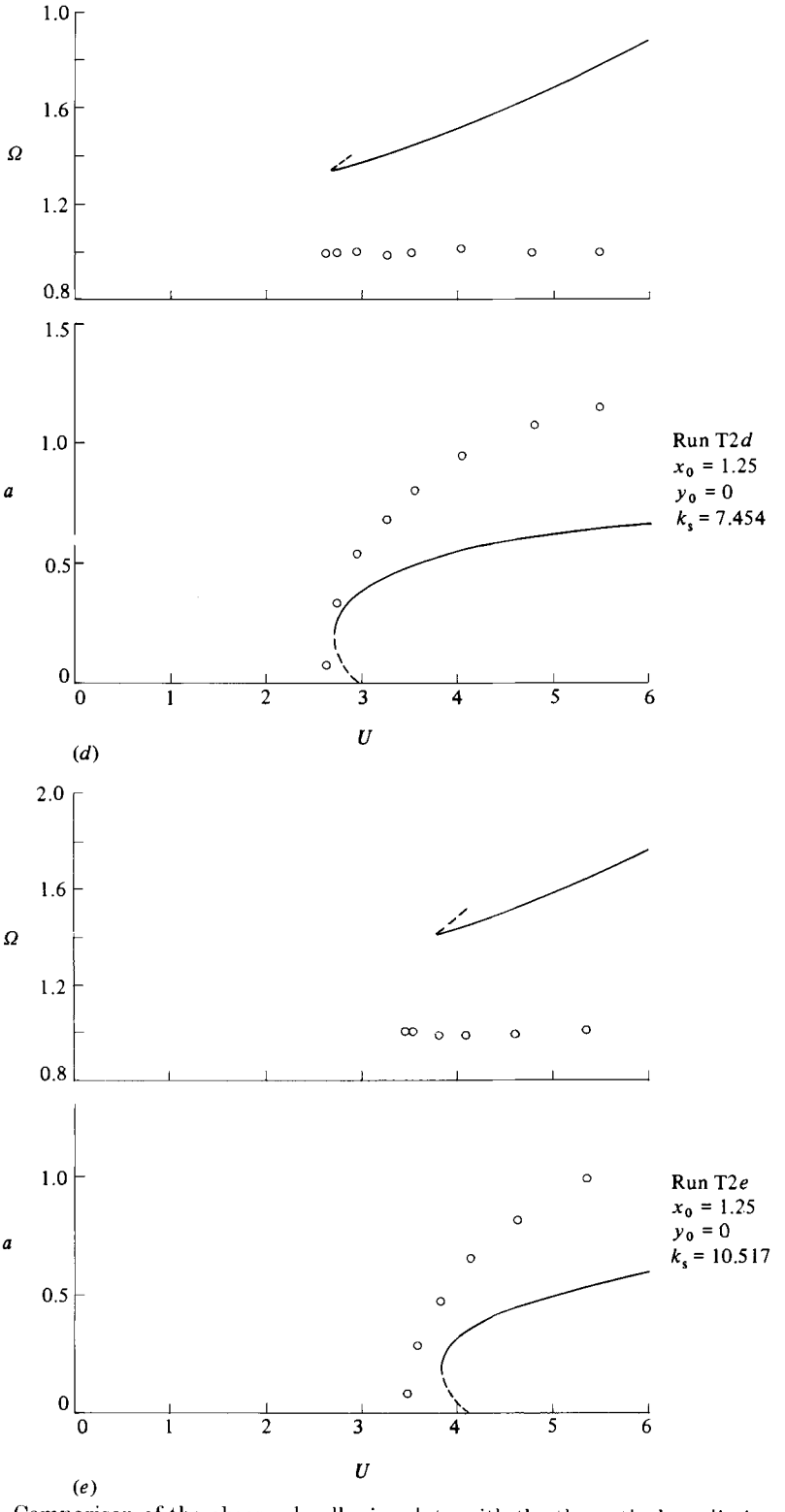

FIGURE 20. Comparison of the observed galloping data with the theoretical predictions: ——, stable response; – – – –, unstable response.

the near wake of the front one. An increase in the flow velocity had no appreciable effect on the extent of the galloping excitation downstream. The vortex-shedding frequency was always found to lock to vibration frequency. It was observed that the galloping amplitudes were sensitive to the cylinders' aspect ratio. An increase in the structural damping only caused the oscillation amplitudes to decrease, and the galloping instability to begin at a higher flow velocity. Whilst some characteristics of proximity-induced galloping were found to be similar to those of galloping of sharp-edged bodies, others were fundamentally different. A quasi-steady theory was developed to predict the galloping behaviour.

This work was undertaken at London Centre for Marine Technology, University College London. The authors are grateful to Professor J. M. T. Thompson for his support and encouragement. F. Geoola is indebted to Mr M. J. Kenn of the Hydraulics Laboratory of Imperial College, London, for generous assistance during the course of this project in that laboratory.

REFERENCES

Blevins, R. D. 1977 *Flow-Induced Vibration.* Van Nostrand Reinhold.

Bokaian, A. & Geoola, F. 1984*a* Hydroelastic instabilities of square cylinders. *J. Sound Vib.* **92**, 117–141.

Bokaian, A. & Geoola, F. 1984*b* Vortex-shedding from two interfering circular cylinders. *Tech. Note, J. Engng Mech. Div. ASCE* **110**, 623–628.

Bokaian, A. & Geoola, F. 1984*c* Wake-induced galloping of two interfering circular cylinders. *J. Fluid Mech.* **146**, 383–415.

Hayes, I. H. 1970 *Numerical Approximation to Functions and Data.* The Athlone Press.

Kiya, M., Suzuki, Y., Arie, M. & Hagino, M. 1982 A contribution to the free-stream turbulence effect on the flow past a circular cylinder. *J. Fluid Mech.* **115**, 151–164.

Kostic, Z. G. & Oka, S. N. 1972 Fluid flow and heat transfer with two cylinders in cross flow. *Intl J. Heat Mass Transfer* **15**, 279–299.

Krylov, N. & Bogoliubov, N. 1949 *Introduction to Non-Linear Mechanics.* Princeton University Press.

Ruscheweyh, H. P. 1983 Aeroelastic interference effects between slender structures. In *Proc. 6th Intl Conf. on Wind Engng, Gold Coast, Australia and Auckland, N.Z.*

Tanida, Y., Okajima, A. & Watanabe, Y. 1973 Stability of a circular cylinder oscillating in uniform flow or in a wake. *J. Fluid Mech.* **61**, 769–784.

Wardlaw, R. L. & Cooper, K. R. 1973 A wind tunnel investigation of the steady aerodynamic forces on smooth and stranded twin bundled power conductors for the Aluminium Company of America. *Natl Aero. Estab., Canada,* LTR-LA-117.

Wawzonek, M. A. & Parkinson, G. V. 1979 Combined effects of galloping instability and vortex-resonance. In *Proc. 5th Intl Conf. on Wind Engng, Fort Collins, Colorado,* vol. 2, pp. 673–684.

Zdravkovich, M. M. 1974 Flow induced vibrations of two cylinders in tandem, and their suppression. In *Proc. Intl Symp. on Flow Structural Vibrations, Karlsruhe 1972,* pp. 631–639. Springer.